fMRI brain activation during a novel VR-based motor imagery and observation task: comparison with a conventional motor imagery task

Poster · October 2020

DOI: 10.13140/RG.2.2.21185.17768

CITATIONS
0

READS
16

8 authors, including:

João Nunes
Instituto Superior Técnico
1 PUBLICATION **0** CITATIONS
SEE PROFILE

Athanasios Vourvopoulos
Instituto Superior Técnico
51 PUBLICATIONS **535** CITATIONS
SEE PROFILE

Carolina Jorge
Madeira Interactive Technologies Institute
6 PUBLICATIONS **27** CITATIONS
SEE PROFILE

Jean-Claude Fernandes
Serviço de Saúde da RAM, E.P.E.
5 PUBLICATIONS **40** CITATIONS
SEE PROFILE

ESMRMB
European Society for Magnetic Resonance in Medicine and Biology

ESMRMB 2020 ONLINE

September 30 - October 2

Book of Abstracts

Friday

DOI: 10.1007/s10334-020-00875-z

www.esmrmb.org

S06 Scientific Session

10:30–12:30 *Room B*

Brain & fMRI

S06.01

Measuring cerebrovascular reactivity in patients with Moyamoya disease: comparison of resting-state BOLD fMRI to breath-hold BOLD fMRI

L. Zerweck[1], T.-K. Hauser[1], C. Roder[2], U. Klose[1]

[1]*University Hospital Tuebingen, Diagnostic and Interventional Neuroradiology, Tuebingen, GERMANY,* [2]*University Hospital Tuebingen, Neurosurgery, Tuebingen, GERMANY*

Introduction: Patients with Moyamoya Disease (MMD) require the estimation of remaining cerebrovascular reactivity (CVR) to evaluate vascular territories at risk of stroke [1]. Positron emission tomography (PET) with acetazolamide (ACZ) challenge is the diagnostic gold standard to assess the CVR. Another, more readily available approach seems to be hypercapnia-triggered BOLD fMRI, for example by breath-holding (bh), where BOLD signal increases are expected in brain tissue with physiological CVR [2]. Recent findings suggest the use of resting-state (rs) BOLD fMRI to estimate the CVR [3]. This approach requires minimum patient compliance and no complex equipment. The aim of this study was to compare rs fMRI to bh fMRI in patients with MMD.

Subjects/methods: The rs fMRI and bh BOLD fMRI data sets of seven patients with angiographically proven MMD were analyzed. All images were acquired on a 3 T MR Scanner. During the rs task the patients were instructed to close their eyes without performing any task. The bh task involved five repetitive cycles, each consisting of 9 s end-expiratory breath-holding and 60 s of regular breathing. The images of both modalities were realigned, normalized, segmented into 6 standardized ROIs [4] and spatially smoothed by a Gaussian kernel of 12 mm FWHM. The bh images were additionally slice-timing corrected. The rs data was temporally filtered with a band-pass filter of 0.02–0.04 Hz, because previous findings suggest that global rs BOLD signal fluctuations within this frequency range correlate best with end-tidal CO_2 fluctuations [3]. The rs CVR maps (Fig. 1a) were calculated by performing a linear regression analysis in which the cerebellar reference time-course was the independent variable and individual voxels signal time-courses were the dependent variable. The bh CVR maps (Fig. 1b) were calculated by voxel-wise integrating the signal time-course averaged over the five cycles.

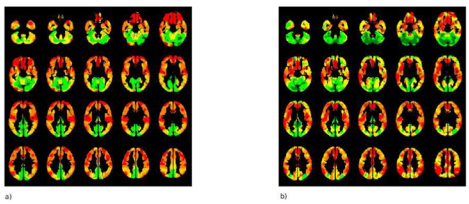

Fig.1 CVR maps of an exemplary patient gained by bh (a) and rs fMRI (b). Colour-coding was applied with low CVR resembled by warm and high CVR by cold colours

The correlation between the normalized rs and bh maps of all patients was calculated, comparing the mean CVR of the standardized ROIs (Fig. 2a).

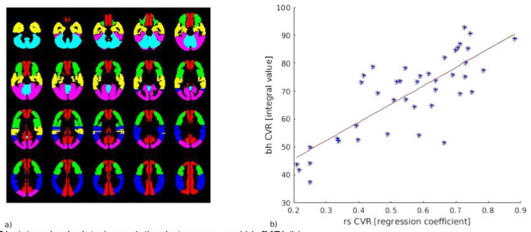

Fig.2 Evaluated ROIs (a) and calculated correlation between rs and bh fMRI (b)

Results/discussion: The present analysis indicates that rs fMRI leads to similar estimation of the CVR to bh fMRI (correlation coefficient = 0.80, $p < 0.001$, Fig. 2b). It seems to be a promising method for hemodynamic evaluation because it is widely available and easily implementable in a high number of patients and therefore merits further research.

References

1. Roder C et al. (2018) World Neurosurg 117:e75–e81.
2. Hauser TK et al. (2019) Neuroimage Clin 22:101713.
3. Liu P et al. (2017) Neuroimage 146:320–326.
4. Tatu L et al. (1998) Neurology 50:1699–1708.

S06.02

Postmortem temperature and its effect on quantitative magnetic resonance imaging

C. Berger, M. Bauer, E. Scheurer, C. Lenz

Institute of Forensic Medicine, Department of Biomedical Engineering, University of Basel, Basel, SWITZERLAND

Introduction: The temperature effect on the magnetic resonance imaging (MRI) parameters T_1, T_2 and T_2* represents a major issue in in situ postmortem MRI (PMMRI) due to the passive cooling of the cadaver [1,2]. A few journal articles were published on this topic [3–6], in which the MRI parameters were corrected for the body core temperature. However, it could be shown that after death the core temperature decreases at a slower cooling rate than the brain temperature [7, 8]. In this study, the effect of the brain and rectal temperature, respectively, on the brain's relaxation parameters were investigated to lay the foundation for future projects on postmortem validation of in vivo MRI techniques.

Subjects/methods: 9 deceased underwent PMMRI brain examination on a 3T scanner using a defined protocol [T1: IR-SE, TE/TR: 12/7060 ms, T2: multi-echo SE, TE/TR: 9.8–117.6/5720 ms, T2*: GRE, TE/TR: 5.79–50.94/68 ms]. The temperatures were measured in situ with temperature probes placed in the rectum and in the brain where it was placed minimally invasive through the nose in-between both brain hemispheres. The temperature effect was computed by fitting a linear model to the MRI parameters of eight different regions of interest and the corresponding brain and rectal temperature, respectively.

Results/discussion: The brain and the core temperature revealed no linear correlation. Significant linear relations between the brain temperature and the relaxation parameters T_1 of the gray matter as well as inter-regional differences were observed (Fig. 1a). While T_2 did not reveal a temperature dependence, T_2* revealed a linear dependence on the brain temperature in deep gray matter (Fig. 1b). The linear correlations assessed with the body core temperature yielded inferior fit results reflected by the RMSE and correlation

coefficient r (Tbl. 1). For white matter significant results could not yet be retrieved as more data sets are needed.

The results highlight the importance of performing accurate post-mortem temperature correction of brain MRI parameters based on the brain temperature instead of the core temperature, particularly of T_1 and T_2*. This will be crucial for future in vivo MRI validation projects in order to avoid misleading quantification caused by postmortem temperature decreases.

PM Temperature [°C]		Frontal Gray matter				Caudate Nucleus				Lentiform Nucleus				Thalamus			
	mean±std.	a	b	RMSE	r	a	b	RMSE	r	a	b	RMSE	r	a	b	RMSE	r
T1																	
Brain	8.9±3.8	0.0068	0.76	0.08	0.82	0.0088	0.68	0.02	0.96	0.0088	0.67	0.04	0.92	0.0059	0.79	0.05	0.81
Core	16.9±9.1	0.0083	0.69	0.07	0.89	0.0096	0.62	0.07	0.80	0.0094	0.62	0.08	0.80	0.0062	0.75	0.06	0.71
T2*																	
Brain	8.9±3.8	0.0036	0.83	0.07	0.27	0.0207	0.26	0.10	0.75	0.014	0.48	0.12	0.70	0.0116	0.59	0.10	0.60
Core	16.9±9.1	0.0047	0.79	0.13	0.44	0.0228	0.14	0.17	0.81	0.0177	0.32	0.14	0.63	0.0119	0.55	0.14	0.65

Table 1: The mean corpse temperature of the brain and the core, and the linear regression parameters (y=ax+b) with the corresponding root mean square error (RMSE) and correlation coefficient r for T1 and T2* of gray matter (where p<0.05).

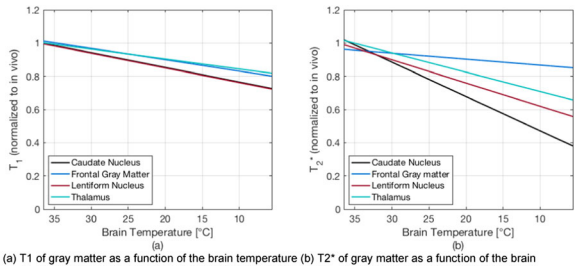

Figure 1: (a) T1 of gray matter as a function of the brain temperature (b) T2* of gray matter as a function of the brain

References

[1] Nelson et al., JMRI, 1987, 189–199, [2] Birkl et al., Magn Reson Med, 2014, 1575–1580, [3] Ruder et al., Eur J Radiol, 2012,1366–1370, [4] Busch et al., J Forensic Sci Med Pat, 2019, 213–217, [5] Tashiro et al., Magn Reson Med Sci, 2015, 51–56, [6] Zech et al., Int J Legal med, 2016, 1071–1080, [7] Bartgis et al., J Therm Biol, 2016, 109–115, [8] Gulyas et al., Neurochem Res, 2006, 157–166

S06.03

Intracellular water lifetime: a new in vivo biomarker of glioma cell invasion/migration by FFC NMR relaxometry

M.R. Ruggiero[1], S. Baroni[1], S.M. Chin[2], S. Aime[1], F. Berger[2], S. Geninatti Crich[1], H. Lahrech[2]

[1]University of Turin, Turin, ITALY, [2]BrainTech Lab INSERM U1205, Grenoble, FRANCE

Introduction: The T_1 of a given tissue changes as a function of the applied magnetic field strength ("T_1-dispersion"). In particular, tumour tissues are characterized by longer T_1 than those of healthy tissues, especially at low magnetic field strengths. The fast field-cycling (FFC)-NMR is the only practicable way of measuring it. An overall increase of water content together with an impairment in water exchange across membranes have fundamental role in this phenomenon. Recent studies show that osmosis- and metabolism-driven movement of free water molecules across membranes (that affect cell volume and shape) may represent an intrinsic and extremely sensitive reporter of the pathology and of its energetic deregulation that is one of the last defined fundamental cancer hallmarks. Recently, FFC-NMR of the invasive glioma tissues of the Glio6 and the Glio96 mouse models are discriminated from solid glioma tissues (U87 model) *ex vivo*[1,2]. The same tendency was also detected in vivo. The aim of this present study was to confirm the involvement of the transmembrane water exchange in this discrimination. The intracellular water residence times (τ_{in}) were quantified in vivo by FFC-NMR relaxometry without exogenous contrast agents[3] .

Subjects/methods: The measurement of τ_{in} was performed in vitro and in vivo on human glioma mouse models (Glio6 and Glio96), developed by BrainTech lab and characterized as models of glioma cell invasion/migration, and on the U87 glioma model, as a standard model of a solid glioma. The data were analysed using two-site exchange (2SX) model[3]in which the Bloch equations are modified to describe two-compartments (intra and extracellular) in which water exchange modulates the observed relaxation behaviour. Immunohistochemistry (IHC) staining for different transporters (AQP4; Na^+/K^+ ATPase) involved in water dynamic cycling and in cancer were performed.

Results/discussion: The R_1-dispersion curves (Fig. 1) show a lower R_1 for Glio6 and Glio96, than U87.

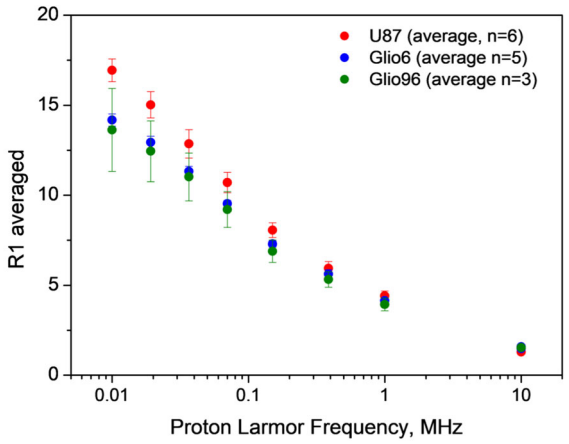

Figure 1: R1 dispersion curve measured in vivo for U87, Glio6 and Glio96 murine model at different magnetic fields

This observation is correlated to a decrease of water exchange rate(τ_{in})in case of invasion models (Fig. 2).

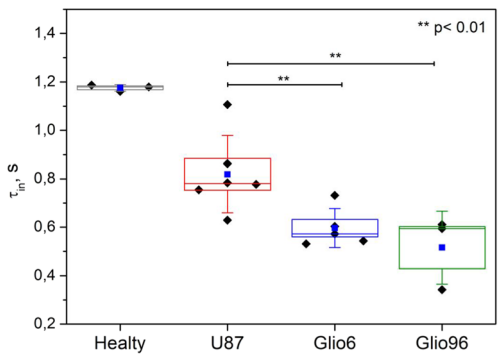

Figure 2: τin values of U87, Glio6 and Glio96 murine mouse model compared to healthy tissue obtained from the data of magnetization decay at 8 different fields fitting to the 2SX model. Errors bars indicate SDs from **P<0.01; Student's t-test.

The H&E (Figure 3a) show a significant different morphology for U87 than Glio6 and Glio96 models. The Na^+/K^+ATPase and AQP4 IHC staining shows a strong positivity for the Glio6 (Fig. 3b).

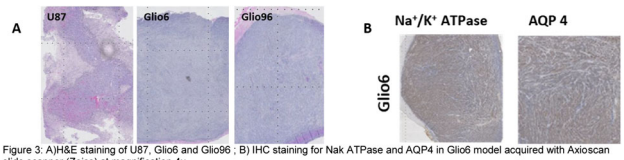

Figure 3: A)H&E staining of U87, Glio6 and Glio96 ; B) IHC staining for Nak ATPase and AQP4 in Glio6 model acquired with Axioscan slide scanner (Zeiss) at magnification 4x

Those results could be a strong effort to explanation about the well-known increase of T_1 at low magnetic fields and here in discriminating between the tissues of glioma invasion and of solid mass formation. Moreover, upregulation of glucose transporters, Na^+/K^+ exchangers, promoted by hypoxia and acidosis, key aspect of an invasive cancer, are also responsible of changes in water exchange rate across cytoplasmatic cell membrane. So, more expression of AQPs and NaK ATPase affects the τ_{in}, that could be confirmed as good tumoral hallmark in glioma tumor too.

References

1. Gimenez, NMR in Biomed (2016)
2. Petit, ISMRM/ESMRMB (2018)
3. Ruggiero, Angew Chem Int Ed Engl (2018)

S06.04

Perfusion imaging with Arterial Spin Labeling (ASL)-MRI predicts malignant progression in low-grade (WHO grade II) gliomas

C.M. Flies[1], T.J. Snijders[1], T. van Seeters[2], M. Smits[3], F.Y.F. de Vos[4], J.W. Dankbaar[2]

[1]University Medical Center Utrecht, Department of Neurology & Neurosurgery, UMC Utrecht Brain Center, Utrecht, NETHERLANDS, [2]University Medical Center Utrecht, Department of Radiology, Utrecht, NETHERLANDS, [3]Erasmus MC, Department of Radiology and Nuclear Medicine, Rotterdam, NETHERLANDS, [4]University Medical Center Utrecht, Department of Oncology, Utrecht, NETHERLANDS

Introduction: Overall survival of patients with a grade II glioma depends on the histomolecular subtype, as defined in the WHO 2016 classification [1]. Degeneration into a higher grade is a key event in its natural history. Predicting such malignant progression (MP) would allow for earlier initiation of appropriate treatment. In this retrospective single-centre case-control study we hypothesised that the perfusion signal on ASL-MRI of grade II gliomas predicts MP in the following 12 months.

Subjects/methods: We included consecutive patients from our institutional database based on the following criteria: 18 years or older, grade II glioma and availability of an ASL-MRI 6–12 months prior to MP (cases) or stable disease (controls). MP was defined either radiologically (new T1-contrast enhancement) or histologically (neurosurgical tissue sampling). Three controls were matched with each case, with cases ideally providing their own control. The ASL-MRIs were reviewed independently by two neuroradiologists. The ASL was classified as positive (hyper-intense or iso-intense compared to cortical grey matter) or negative (hypo-intense). In patients with active epilepsy, a neurologist reviewed clinicoradiological data to exclude peri-ictal pseudoprogression. The statistical analysis included an odds ratio (OR) with 95%-confidence interval (95% CI), a Chi square test, sensitivity, specificity and a Cohen's Kappa interrater reliability coefficient between the neuro-radiologists. We performed an additional analysis of diagnostic value with stratification for previous radiotherapy.

Results/discussion: 11 cases and 33 controls were selected (36 patients, 45 ± 22 years, 23 men). 29 ASL-MRIs were assessed as negative and 15 as positive. MP appeared after a median of 37 ± 27 months after first surgery. Cohen's Kappa was 0.65. For the whole group, ASL significantly predicted subsequent MP (sensitivity 72.7%, specificity 78.8%, OR 9.9, 95% CI 2.1–47.5). In the stratified analysis, ASL-MRI predicted MP both in patients with previous RT and in those without (pooled OR 11.2, 95% CI 2.1–59.3). None of the MRIs were judged to show signs of peri-ictal pseudoprogression.

In conclusion, perfusion imaging with ASL-MRI can predict MP within the next 12 months in untreated and treated patients with grade II gliomas. The generalisability of these results needs to be confirmed in a larger prospective multi-centre cohort study. Based on current results, we advise to follow patients with grade II glioma and a positive ASL-MRI closely for subsequent MP.

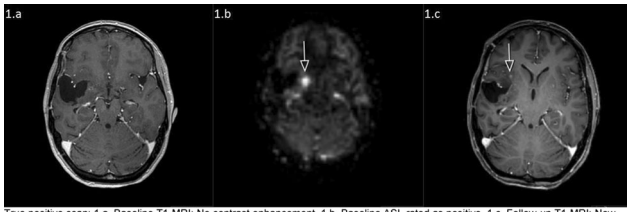

True positive scan; 1.a. Baseline T1-MRI: No contrast enhancement. 1.b. Baseline ASL rated as positive. 1.c. Follow-up T1-MRI: New contrast enhancement.

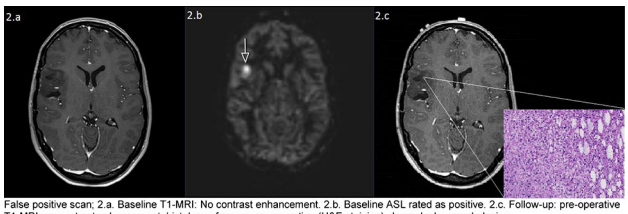

False positive scan; 2.a. Baseline T1-MRI: No contrast enhancement. 2.b. Baseline ASL rated as positive. 2.c. Follow-up: pre-operative T1-MRI, no contrast enhancement, histology of recurrence resection (H&E staining) showed a low-grade lesion.

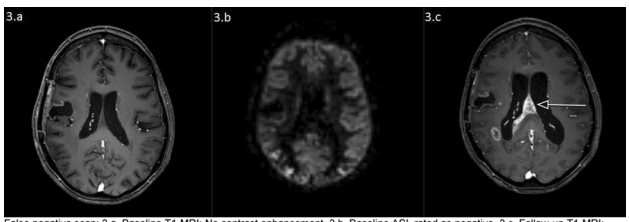

False negative scan; 3.a. Baseline T1-MRI: No contrast enhancement. 3.b. Baseline ASL rated as negative. 3.c. Follow-up T1-MRI: New contrast enhancement.

References

1. Louis, D.N., Perry, A., Reifenberger, G., von Deimling, A., Figarella-Branger, D., Cavenee, W. K., Ohgaki, H., Wiestler, O.D., Kleihues, P., Ellison, D.W., The 2016 World Health Organization Classification of Tumors of the Central Nervous System: a summary. Acta Neuropathol, 2016. 131(6): p. 803–20 https://doi.org/10.1007/s00401-016-1545-1.

S06.05

Variations in brain magnetic susceptibility in sickle cell anaemia

R. Murdoch[1], J. Kawadler[2], F. Kirkham[2], K. Shmueli[1]

[1]University College London, Medical Physics and Biomedical Engineering, London, UNITED KINGDOM, [2]University College London, Great Ormond Street Institute for Child Health, London, UNITED KINGDOM

Introduction: Sickle Cell Anaemia (SCA) is an inherited blood disorder, characterized by haemolytic anaemia, vasculopathy, and cognitive impairment. Brain iron is important in cognitive function and the effect of SCA upon brain iron is not clear. Quantitative susceptibility mapping (QSM) studies have shown strong correlations between magnetic susceptibility (χ) and iron concentration in deep grey matter (GM), and myelin is a significant white matter (WM) χ source. A recent QSM study suggests increased iron accumulation with age in deep GM regions in SCA relative to healthy controls (HC)[2]. Here, we investigated changes in χ throughout the brain.

Subjects/methods: 83 SCA subjects (mean $\pm$ σ age: 18.57 $\pm$ 10.84 years) and 23 HC (16.36 $\pm$ 5.02) were imaged on a 3T Siemens Magnetom Prisma System. QSM was calculated using a previously described pipeline[3] applied to multi-echo gradient echo (ME-GRE) images with seven echoes, $TE_1/\Delta TE/TR$: 3/4/38 ms and 1.15 mm^3 isotropic resolution.χ variations were investigated as follows: Study-wise template was created from 1 mm^3 isotropic T1-weighted MP-RAGE images using ANTs' diffeomorphic Greedy-Syn model[4]. χ maps were co-registered to the study-wise template, using transformations calculated from ME-GRE magnitude images, and smoothed (σ = 3 mm). Both the absolute $\chi(|\chi|)$, as in previous studies, and positive and negative $\chi(\chi_{true})$ were investigated. Differences between SCA and HC groups were tested using FSL randomize. An exponential age model was used (age range: 8.4–63.9 years). We examined four contrasts for both $|\chi|$ and χ_{true}: (1) Increase in χ with Ln(age). (2) Decrease in χ with Ln(age). (3) Increased χ in SCA v. HC. (4) Decreased χ in SCA v. HC. Significant regions were identified at the $p < 0.05$ level corrected for the false discovery rate.

Results/discussion: An increase in $|\chi|$ with age was observed in several GM and WM clusters (Fig. 1). No decreases in $|\chi|$ with age were observed. Regions where $|\chi|$ increased with age could be split into voxels where χ_{true} increased in GM, consistent with iron accumulation, and χ_{true} decreased in WM, consistent with myelination.

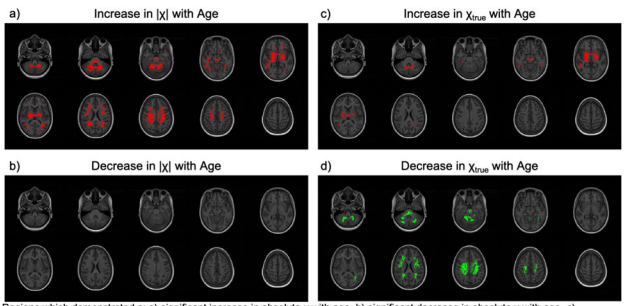

Regions which demonstrated a: a) significant increase in absolute χ with age. b) significant decrease in absolute χ with age. c) significant increase in true χ with age. d) significant decrease in true χ with age. Significant at FDR corrected $p<0.05$.

Comparing χ_{true} and $|\chi|$ results allows detection of whether positive or negative χ values are increased or decreased in SCA versus HC (Fig. 2). Higher positive χ in SCA was observed in a few deep GM regions, suggesting increased iron content. Lower positive χ in SCA was observed in the thalamic area, suggesting decreased iron content. Less negative χ in SCA was found close to the GM-WM boundary where silent cerebral infarcts (SCI) are common and could represent demyelination or iron accumulation. The ability to disentangle positive and negative χ differences in white and grey matter regions demonstrates the importance of examining whole-brain changes in both $|\chi|$ and χ_{true}.

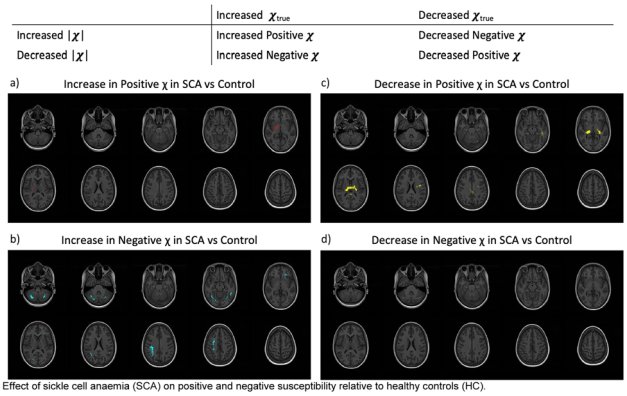

Effect of sickle cell anaemia (SCA) on positive and negative susceptibility relative to healthy controls (HC).

References

1. Langkammer C, et al. NeuroImage 2012
2. Miao X, et al. Blood. 2018
3. Murdoch R, et al. ISMRM 2019 #5066
4. Avants B, et al. Med Image Analysis. 2008

S06.06

Increased cerebrovascular reactivity during spontaneous migraine attacks compared to pain-free periods

S. Cotrim[1], R. Gil-Gouveia[2], J. Pinto[3], P. Vilela[2], I. Pavão Martins[4], P. Figueiredo[1]

[1]Instituto Superior Técnico, Universidade de Lisboa, ISR-Lisboa/LARSys and Department of Bioengineering, Lisbon, PORTUGAL, [2]Hospital da Luz, Lisbon, PORTUGAL, [3]University of Oxford, Institute of Biomedical Engineering, Department of Engineering Science, Oxford, UNITED KINGDOM, [4]Faculdade de Medicina, Universidade de Lisboa, Department of Clinical Neurosciences, Lisbon, PORTUGAL

Introduction: Migraine is a disabling neurological condition, characterized by intermittent headache attacks (ictal phase) alternating with pain-free (interictal) periods[1]. Cerebrovascular reactivity (CVR) has been shown to be altered in the brain of migraineurs and evidence of endothelial dysfunction in these patients is growing[2]. However, only one of these studies used fMRI, and only two analysed both ictal and interictal phases[3,4]. Here, we use BOLD-fMRI with breath-holding (BH) to measure CVR during spontaneous migraine attacks and pain-free periods.

Subjects/methods: 11 female patients (36 $\pm$ 7 years) with episodic migraine without aura were studied on a 3T Siemens scanner (12-channel RF coil), on two sessions: during ictal and interictal phases. BOLD-fMRI data were acquired (2D GE-EPI, TR/TE = 2500/50 ms, 3.5 $\times$ 3.5 $\times$ 7.0 mm^3) during a BH task (3 cycles of 20 s BH alternated with normal breathing).

Image analysis was conducted in FSL and MATLAB. Preprocessing included motion correction, distortion correction, spatial smoothing, highpass temporal filtering and registration (to MPRAGE and MNI). A general linear model analysis was performed (sine and cosine waves at task frequency and their 1st and 2nd harmonics; motion

parameters and outliers) and the amplitude (CVR, percent signal change) and time-to-peak (TTP) of the BH BOLD response were computed[5]. Group-level analysis was performed to identify differences in CVR and TTP between ictal and interictal phases. Pearson correlation analysis was performed between the individual mean CVR and TTP and the pain duration (time between attack onset and data acquisition).

Results/discussion: Representative CVR and TTP maps are shown in Fig. 1. Group-analysis revealed increased CVR and TTP in occipital regions during the attack (Fig. 2). Ictal CVR and TTP values showed a higher dispersion than interictal ones (Fig. 3-Left), which may be explained by the fact that patients were studied at different times during the attack; this is supported by the negative correlation found between ictal CVR and pain duration (Fig. 3-Right).

The increased CVR and TTP observed in occipital regions during attacks is consistent with the reduced reactivity of the posterior cerebral circulation reported in the interictal phase of migraineurs relative to controls using Doppler ultrasound[6], and also with the presence of ischemic-like lesions in the posterior circulation of migraineurs[7,8]. Future work should compare both ictal and interictal phases of migraineurs with healthy controls to test the hypothesis of a reduced interictal CVR that increases during attacks.

References

Goadsby, *PhysiolRev* 97.2(2017):553–622
Hoffmann, *JJCBFM* 39.4(2019):573–94
Harer, *JNeurol* 238.1(1991):23–26
Sakai, *Headache* 19.5(1979):257–66
Pinto, *Neuroimage* 135(2016): 223–2+31
Perko, *ActaNeurolScand* 124.4(2011):269–74
Kruit, *Brain* 128.9(2005):2068–77
Milhaud, *Neurology* 57.10(2001):1805–11

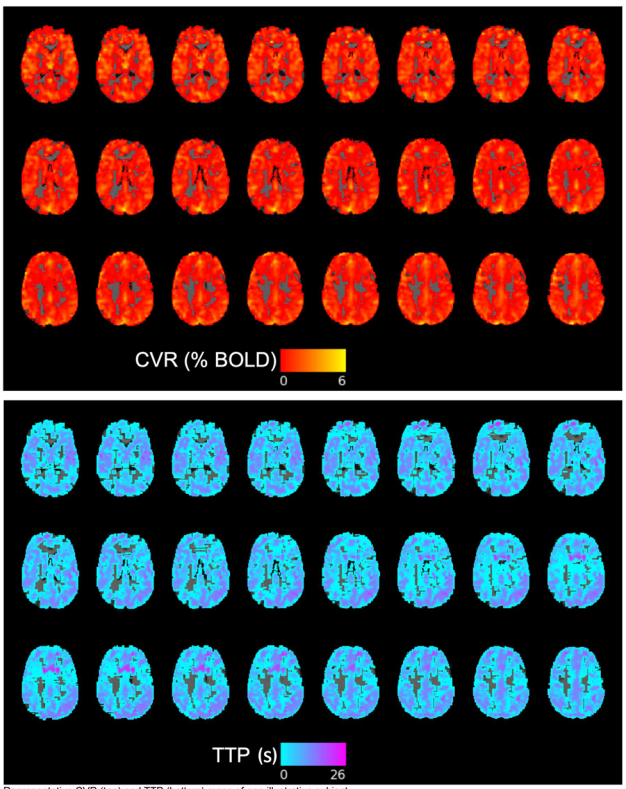

Representative CVR (top) and TTP (bottom) maps of one illustrative subject.

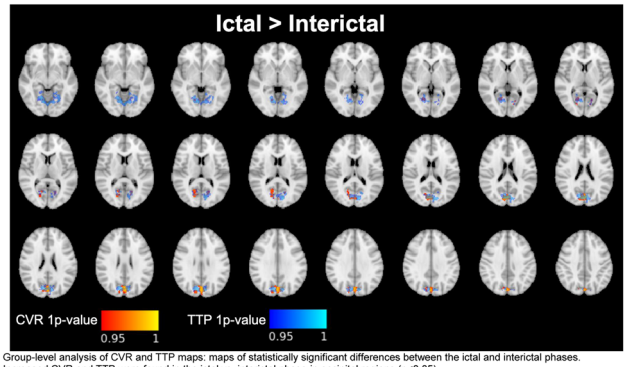

Group-level analysis of CVR and TTP maps: maps of statistically significant differences between the ictal and interictal phases. Increased CVR and TTP were found in the ictal vs. interictal phase in occipital regions (p<0.05).

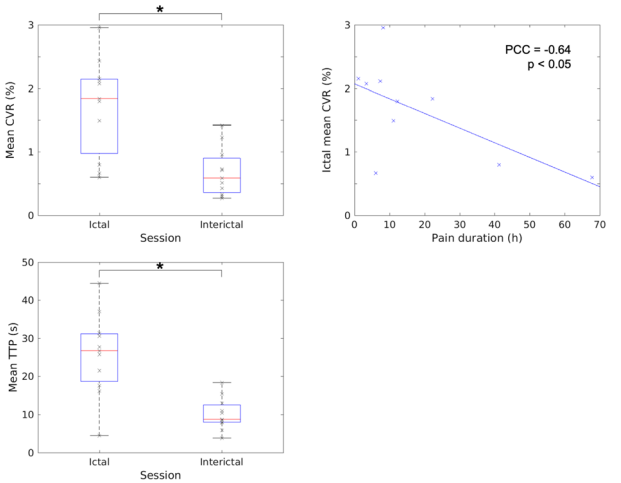

(Left)Distributions of mean ictal and interictal CVR and TTP values within the ictal>interictal ROI shown in Fig.2(*p<0.05). (Right)Post-hoc Pearson correlation analysis: ictal mean CVR values are negatively correlated with pain duration.

S06.07

fMRI brain activation during a novel VR-based motor imagery and observation task: comparison with a conventional motor imagery task

J. Nunes[1], A. Vourvopoulos[1], D. Blanco-Mora[2], C. Jorge[3], J.-C. Fernandes[3], S. Fernandes[4], S. Bermúdez i Badia[5], P. Figueiredo[1]

[1]Institute for Systems and Robotics, Lisboa, Department of Bioenineering, Instituto Superior Técnico, Universidade de Lisboa, Lisboa, PORTUGAL, [2]Madeira Interactive Technologies Institute, Universidade da Madeira, Funchal, PORTUGAL, [3]Central Hospital of Funchal, Physical Medicine and Rehabilitation Service, Funchal, PORTUGAL, [4]Central Hospital of Funchal, Neuroradiology Unit, Funchal, PORTUGAL, [5]Madeira Interactive Technologies Institute and Faculdade de Ciências Exatas e da Engenharia, Universidade da Madeira, Funchal, PORTUGAL

Introduction: We have previously developed a novel VR-based motor imagery (MI) and motor observation (MO) task targeting the upper limbs for stroke rehabilitation-NeuRow; it consists of imagining the kinaesthetic experience of rowing using the left or right arm [1]. Here, we evaluate brain activation elicited by NeuRow and compare it with an abstract MI task using the conventional Graz paradigm.

Subjects/methods: Two groups of healthy right-handed subjects participated: 10 young adults (27 ± 4 years); and 10 older subjects (51 ± 6 years). Imaging was performed on a 3T GE Signa HDxt MRI

scanner using a 12-channel RF coil. fMRI used 2D EPI (TR/TE = 2500/30 ms, 3.75 × 3.75 × 3.00 mm^3 voxel size).

Subjects underwent four fMRI runs (each consisting of 8 cycles, alternating 20 s blocks of task and baseline, total 5.33 min) under the following conditions (pseudo-randomized order): (1) left Graz-MI; (2) right Graz-MI; (3) left NeuRow; and (4) right NeuRow. for Graz-MI, an arrow indicated the arm movement (left/right) to imagine, while for NeuRow, a two-armed virtual avatar executed the intended movement (left/right).

Data analysis was performed using FSL (fsl.fmrib.ox.ac.uk). After pre-processing (motion correction, spatial smoothing, highpass temporal filtering) and registration (to MNI space), a general linear model including the task and six motion parameters as confounds was fitted to the data. For each task, a two-sample unpaired *t* test was used to assess differences between groups. Since no significant differences were found, a repeated-measures ANOVA was used to assess differences between sides (left/right arm) and condition (Graz-MI/NeuRow) for the whole subject cohort. All statistical maps were converted into Z-Scores and submitted to cluster thresholding (voxel $Z > 3.1$; cluster $p < 0.05$) to correct multiple comparisons.

Results/discussion: Figure 1 shows the mean group activation for each fMRI run. Left and right arms showed significant differences as expected (not shown). Figure 2 shows the brain regions exhibiting significantly different activation between NeuRow and Graz-MI; Table 1 describes them in detail. Compared to Graz-MI, NeuRow activated more occipital and parietal regions.

Our findings are in line with the literature of MI and MO tasks, which report activation of parietal and occipital areas more consistently kindred with MO than MI [2]. Besides, we found no age-related differences, in concordance with a previous study demonstrating that MI ability is not affected up to 70 years [3]. Overall, our results indicate that NeuRow may be more powerful than conventional MI in the context of neurorehabilitation, by more strongly engaging brain areas associated with the mirror neuron and sensorimotor systems [4].

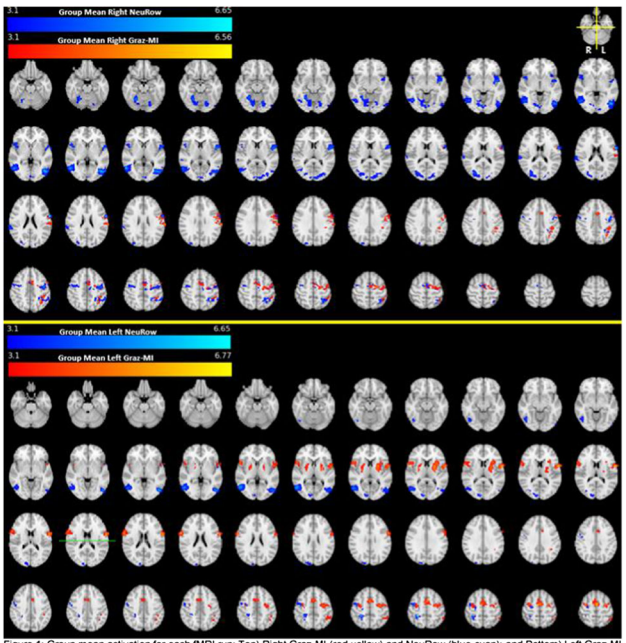

Figure 1: Group mean activation for each fMRI run: Top) Right Graz-MI (red-yellow) and NeuRow (blue-cyan); and Bottom) Left Graz-MI (red-yellow) and NeuRow (blue-cyan). Thesholded Z stats maps (colour) are overlaid on the MNI T-weighted image.

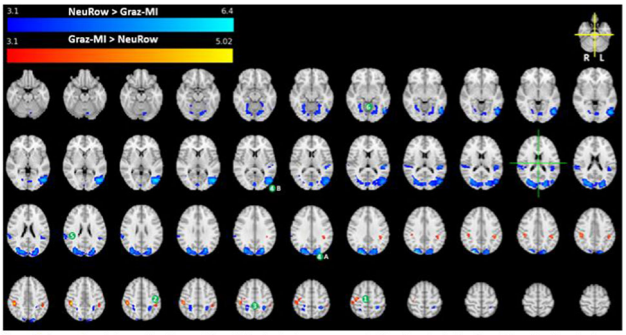

Figure 2: Comparison between NeuRow and Graz-MI tasks: brain areas more significantly activated by Graz-MI vs. Neu Row (red-yellow) and NeuRow vs. Graz-MI (blue-cyan). Identified brain areas are described in Table 1.

Brain Regions	Z peak MNI coordinates [mm] x	y	z	Z peak value	Cluster Size (number of voxels)
Graz-MI>NeuRow					
1: Supramarginal Gyrus, Anterior Division, Precentral Gyrus and Postcentral Gyrus (Right)	23	47	58	5,02	360
2: Supramarginal Gyrus, Anterior Division, Postcentral Gyrus (Left)	67	46	56	4,29	240
NeuRow>Graz-MI					
3: Superior Parietal Lobule (Right)/ Primary Somatosensory Cortex	32	37	62	4,04	175
3: Superior Parietal Lobule (Left)/ Primary Somatosensory Cortex	59	41	63	5,03	201
4A: Lateral Occipital Cortex, Posterior Division , 4B: Lateral Ocipital Cortex Inferior Division /Visual Cortex	67	26	38	6,4	5247
5: Supramarginal Gyrus, Posterior Division Planum Temporale, Parietal Opercular Cortex/ (Right)	11	46	48	4,75	345
5: Supramarginal Gyrus, Posterior Division; Planum Temporale, Parietal Opercular Cortex /(Left)	69	48	42	5,33	348
6: Temporal Occipital Fusiform Cortex, Occipital Fusiform Gyrus	30	35	41	4,55	905

Table 1. Comparison between NeuRow and Graz-MI tasks: brain areas more significantly activated by Graz-MI vs. Neu Row (top) and NeuRow vs. Graz-MI (bottom); Local maxima (Z peak) MNI coordinates and respective Z value and cluster volume.

References

1. Vourvopoulos, Front Hum Neurosci, 3:1–17, 2019
2. Hardwick, Neurosci Biobehav Rev, 94:31–44, 2018
3. Schott, Exp Aging Res, 38(5):559–583, 2012
4. Garrison, Neurorehabil Neural Repair, 24(5):404–412, 2010

S06.08

Spiral in/out trajectory with GIRF prediction for passband bSSFP fMRI at 7T

M. Veldmann, P. Ehses, T. Stöcker

Deutsches Zentrum für Neurodegenerative Erkrankungen e.V., MR Physics, Bonn, GERMANY

Introduction: Functional MRI (fMRI) requires fast acquisition times in order to reach high temporal resolutions. Spiral k-space trajectories are well suited for fMRI as they are among the fastest ways of covering k-space [1]. However, spiral acquisitions suffer from gradient imperfections as knowledge of the exact k-space trajectory is crucial for reconstruction. This can be solved by using the Gradient Impulse Response Function (GIRF) for prediction of actual k-space trajectories [2, 3], requiring only a one-time calibration measurement.

A spiral trajectory was implemented in a balanced Steady State Free Precession (bSSFP) sequence at 7T and applied in an fMRI experiment. In contrast to the T2* BOLD contrast of commonly used spoiled gradient echo sequences, the bSSFP sequence produces a T2 BOLD contrast more selective to smaller vessels [4, 5].

Subjects/methods: All measurements were performed on a Siemens MAGNETOM Terra 7T scanner. Images were acquired with a 3D stack of spirals acquisition with 27 interleaves per fully sampled spiral set (Fig. 1). A GIRF predicted spiral in/out trajectory was used as it is less prone to offresonances compared to a spiral out readout [6]. For further artifact reduction, every second image was acquired with a flipped trajectory and after reconstruction combined with the previous image [7]. The GIRF was measured with a field camera (Skope) and a sequence of triangular gradients as proposed in [8]. Spiral Trajectories were tested with different acceleration factors R and CAIPIRINHA shifts δ (Fig. 2) at an in-plane resolution of 1 mm. Visual stimulation was achieved by presenting a flickering checkerboard ten times for 15 s, with 15 s of rest between each stimulus. Functional data were acquired with the following parameters: TR = 7 ms, FA = 13°, FoV = 210 × 210 × 40 mm^3, Res = 1 mm × 1 mm × 2 mm, R = 3, δ = 2. This resulted in an acquisition time (TA) of 1.26 s per volume (total TA = 5 min). Image reconstruction was done with the Berkeley Advanced Reconstruction Toolbox [9], fMRI analysis with FSL [10].

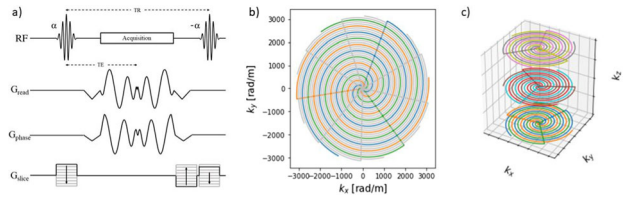

Fig1: a) 3D spiral in/out bSSFP sequence with slab-selective excitation. b) 2D k-space trajectory - grey interleaves display an acceleration factor of R=3. c) Stack of spirals with CAIPIRINHA shift in subsequent partitions.

Results/discussion: Reconstructed bSSFP images in Fig. 2 are of high quality even at a relatively high acceleration factor of R = 5. The GIRF prediction was essential to reduce trajectory related artifacts in the images. In the frontal lobe of the brain a small banding artifact is visible, however, far away from the visual cortex.

Z-score maps of the fMRI experiment in Fig. 3 show a high BOLD contrast in the visual cortex related to the stimulation. Further acceleration resulting in a higher temporal resolution is possible by reducing the number of spiral interleaves or by additional acceleration along the phase encoding dimension.

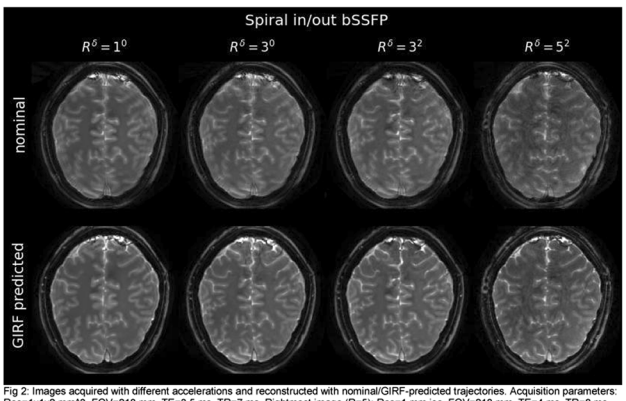

Fig 2: Images acquired with different accelerations and reconstructed with nominal/GIRF-predicted trajectories. Acquisition parameters: Res=1x1x2 mm^3, FOV=210 mm, TE=3.5 ms, TR=7 ms. Rightmost image (R=5): Res=1 mm iso, FOV=210 mm, TE=4 ms, TR=8 ms.

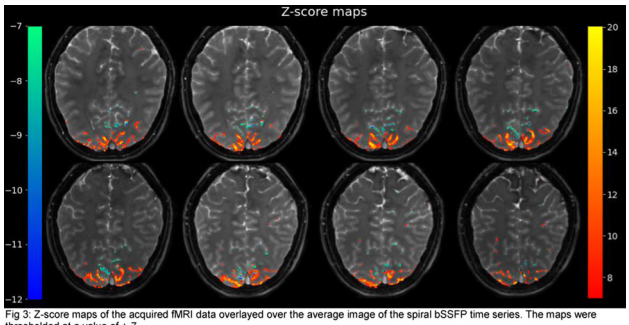

Fig 3: Z-score maps of the acquired fMRI data overlayed over the average image of the spiral bSSFP time series. The maps were thresholded at a value of +-7.

References

[1] Glover, NI, 2012
[2] Vannesjo, MRM, 2016
[3] Addy & Nishimura, MRM, 2012
[4] Bieri & Scheffler, NMR Biomed, 2007
[5] Miller, NI, 2012
[6] Glover, MRM, 2001
[7] Fielden & Meyer, MRM 2015
[8] Vannesjo, MRM, 2013
[9] Uecker, MRM, 2014
[10] Woolrich, NI, 2001

S06.09

Arterial blood contrast (ABC) enabled by magnetization transfer (MT): a novel MRI technique for enhancing the measurement of brain activation changes beyond BOLD

J. Schulz, Z. Fazal, R. Metere, J.P. Marques, D.G. Norris

Radboud University Nijmegen, Donders Institute for Brain, Cognition and Behaviour, Nijmegen, NETHERLANDS

Introduction: Functional brain imaging in humans is almost exclusively performed using blood oxygenation level dependent (BOLD) contrast. This typically requires a period of tens of milliseconds after excitation of the spin system to achieve maximum contrast leading to inefficient use of acquisition time, reduced image quality, and inhomogeneous sensitivity throughout the cortex. We utilise magnetisation transfer (MT)[1] to suppress the signal differentially from grey matter relative to blood so that the local increase in blood volume associated with brain activation (mainly occurring in the arterioles and capillaries) will increase the measured signal[2–7]. Arterial blood contrast (ABC) is additive to the residual BOLD effect but will have its maximum value at the time of excitation.

In this work, we measured brain activation using combined ABC and residual BOLD contrast at different times post-excitation (MT-on) and compared this to a standard BOLD (MT-off) experiment.

Subjects/methods: We used a 2D ME GE-EPI sequence with an MT preparation consisting of two net 0° non-sel. binomial pulses (± 77°/∓154°/± 77°) plus a random gradient spoiler scheme. Data were acquired from 16 subjects on a 3T Siemens Prisma using a simple visual stimulus block design of a hemifield checkerboard flickering at 4 Hz [10 s on, 26–32 off ISI]. Acquisition parameters are shown in Table 1.

	TEs (ms)	TR (ms)	res (mm)	matrix	iPAT	PF	FA	BW (Hz/px)	TA (min)
ME-GE EPI	6.9/18/28	2000	3x3x3	80x80	3	6/8	50°	2718	10:00

Table 1: Protocol parameters. There were identical parameters for MT-on and MT-off acquisition with the MT pulse turned off in the MT-off case.

The hemifield specific contrast, *R-L*, for MT-on/off was analysed using FSL 6.0.1. Group-level results were obtained using mixed-effect statistics. The union of MT-on$_{TE=6.9}$ and MT-off$_{TE=28}$ group-level activation maps were used to define the activated region of interest (ROI).

Results/discussion: Figure 1 shows how the activation patterns vary as a function of TE for the two contrasts. Significant activation is obtained at shorter echo times (TE = 6.9/18 ms) for the MT-on experiment but not for MT-off.

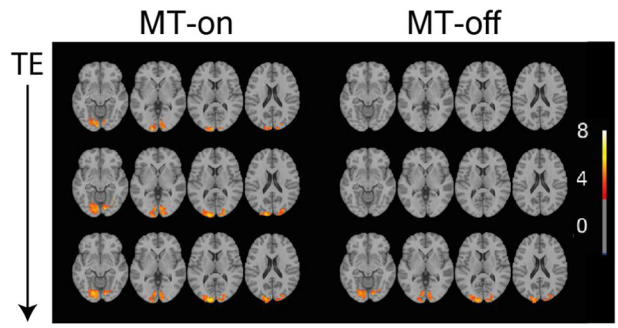

Figure 1: Group-level activation maps within the visual cortex, for all three TE-values (6.9/18/28ms). All echo times show MT-on activation, whereas there is no statistically relevant activation for MT-off, except at TE=28ms showing BOLD contrast.

Figure 2 shows the mean z-scores of activated voxels within the defined ROI as a measure of functional sensitivity as well as the total number of significantly activated voxels (thresholded $z > 3.1$). With MT-on, we obtain the highest z-scores at TE = 18 ms and get similar numbers of activated voxels and z-scores at all TEs. In comparison, the MT-off experiment shows the typical behaviour of BOLD contrast showing significant activation only at TE = 28 ms. Similar z-score values are obtained for MT-on$_{TE=6.9}$ (3.6 ± 0.3) and MT-off$_{TE=28}$ (3.6 ± 0.3), but there are slightly more activated voxels for MT-off$_{TE=28}$ (3035) compared to MT-on$_{TE=6.9}$ (2517).

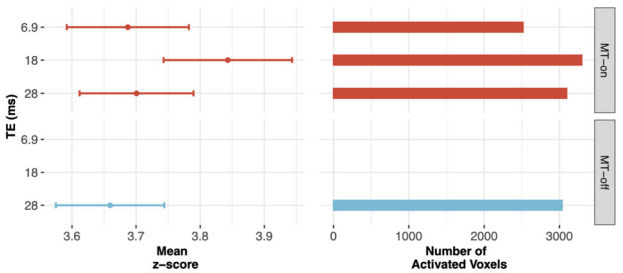

Figure 2: Mean z-scores and number of activated voxels within ROI defined by the MT-off(TE=28ms) activation map. Mean z-scores are calculated only for pixels showing significant activation at z>3.1.

We conclude that using ABC and measuring shortly after excitation gives comparable sensitivity to standard BOLD but will provide greater efficiency, spatial specificity and improved image quality. ABC offers new perspectives for performing functional MRI.

References

1. Wolff et al. MRM, 1989
2. Balaban et al. Radiology, 1991
3. Zhang et al. MRM, 1997
4. Song et al. NMR in Biomed, 1997
5. Zhou et al. MRM, 2005
6. Kim and Kim. MRM, 2005
7. Kim et al. MRM, 2008

S06.10

Abnormal dynamic functional connectivity state in cerebral small vessel disease

M. Palma[1], J. Pinto[2], J. Cabral[3], A. Fouto[1], L. Alves[4], S. Calado[4], M.V. Baptista[4], P. Vilela[4], P. Figueiredo[1]

[1]ISR-Lisboa/LARSyS and Department of Bioengineering, Instituto Superior Técnico – Universidade de Lisboa, Lisboa, PORTUGAL, [2]Institute of Biomedical Engineering, Department of Engineering Science, University of Oxford, Oxford, UNITED KINGDOM, [3]Life and Health Sciences Research Institute (ICVS), School of Medicine, University of Minho, Minho, PORTUGAL, [4]Neurology Department, Hospital Egas Moniz, Centro Hospitalar de Lisboa Ocidental; CEDOC, Nova Medical School, New University of Lisbon, Lisboa, PORTUGAL

Introduction: Cerebral small vessel disease (SVD) encompasses all pathological processes affecting the small brain vessels and it is associated with progressive cognitive impairments [1]. Resting-state functional magnetic resonance imaging (rs-fMRI) has demonstrated potential to deliver sensitive biomarkers of SVD, by revealing disruptions in functional connectivity (FC) across brain networks [3]. However, so far only one study has explored the commonly observed FC temporal fluctuations—so-called dynamic FC (dFC) [2]. Here, we aim to further investigate dFC in SVD by employing the Leading Eigenvector Dynamics Analysis approach [3] to identify dFC states that differ from healthy controls (HC).

Subjects/methods: 17 SVD patients (50 ± 9 years) and 12 HCs (47.2 ± 11 years) were studied using rs-fMRI (2D-GE-EPI, TE/TR = 30/2500 ms, 3.5 × 3.5 × 3.0 mm^3, ~ 6.5 min, eyes open) on a 3T Siemens scanner. Data were analysed using FSL and MATLAB. Preprocessing included motion correction, spatial smoothing (FWHM = 5 mm), nuisance regression of motion outliers, ICA denoising, bandpass temporal filtering (0.01–0.1 Hz), and registration to MNI space. After parcellation using the AAL atlas, the phase of the region-averaged BOLD signals was estimated using the Hilbert transform and phase coherence (PC) was computed between each pair of regions at each time point, yielding a time-resolved dFC matrix. To analyse dFC patterns over time and subjects, only the leading eigenvector of each dFC matrix was considered, and k-means clustering was applied to estimate k clusters each representing a recurrent dFC pattern, or state. k was varied between 2 and 20, and the occurrence probability and lifetime of each state were computed. For each k = 2…20, and each state 1…k, a permutation-based paired t-test with Bonferroni correction for multiple comparison was used to identify significant differences between SVD and HC groups.

Results/discussion: The dFC states estimated for k = 1–11 are presented in Fig. 1. For k = 10, 1 of the 10 dFC states was identified as having a significantly higher occurrence probability in SVD relative to HC (Fig. 2). This dFC state comprises frontal and parietal areas and is significantly associated with the somatomotor, dorsal attention and ventral attention networks (Fig. 3), as assessed by correlation with well-established resting-state networks [4]. The altered connectivity between parietal and frontal brain regions may be related with deficits in the integration of sensory information [1]. Our results agree with those of the only previous report of dFC in SVD [2]. Indeed, we

also found that the abnormal dFC state was more weakly connected than the others (Fig. 2-B). Overall, our study indicated that dFC may provide sensitive biomarkers of SVD, and should be further explored in terms of its potential to predictive cognitive decline.

References

[1] Telgte, Nat Rev Neurol 14, 2018
[2] Fu, HBM 40, 2019
[3] Cabral, Sci Rep 7, 2017
[4] Yeo, JNP 106, 2011

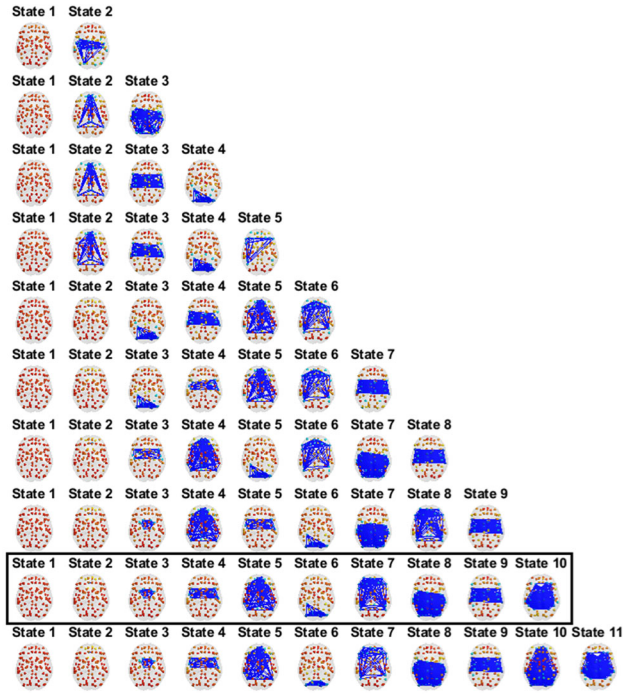

Fig.1: Representation of the dFC states (from k=2, top, to k=11, bottom) in AAL space.

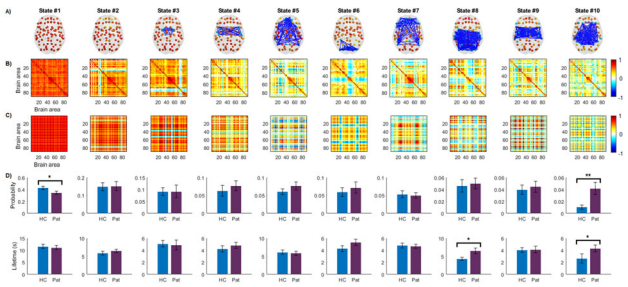

Fig.2: dFC states for k=10.(A) Representation in AAL space.(B) dFC matrix.(C) Probability of occurrence and lifetime in SVD and HC.(**significant group differences with correction for multiple comparisons).(D) Outer product of dFC centroid vector.

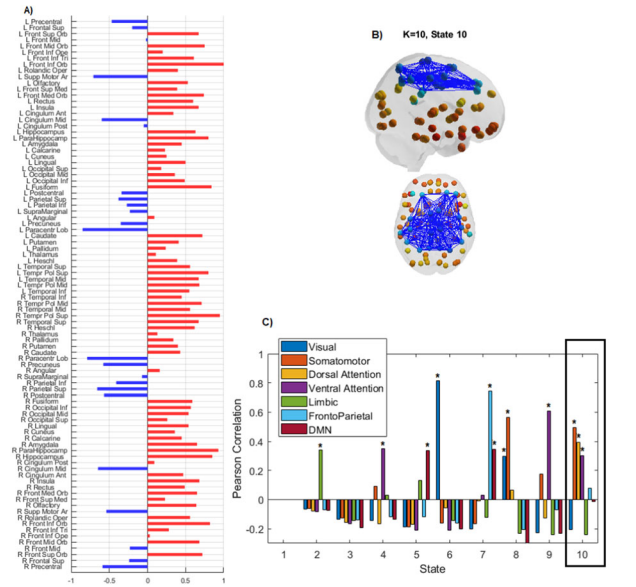

Fig.3: dFC state with a significantly higher occurrence probability in SVD vs HC.(A) dFC state centroid vector with indication of the AAL regions.(B) Representation in AAL space.(C) Correlation of the dFC state with each of the 7 RSNs [4].

S06.11

Comparison between pulsed and pseudo-continuos arterial spin labeling with single-shot 3D GRASE readout for fMRI at 3T

D. Ivanov[1], J. Pfeuffer[2], A. Gardumi[1], K. Uludağ[3], B. Poser[1]

[1]Maastricht University, Department of Cognitive Neuroscience, Maastricht, NETHERLANDS, [2]Siemens Healthineers, Erlangen, GERMANY, [3]Techna Institute & Koerner Scientist in MR Imaging, University Health Network, Toronto, CANADA

Introduction: Arterial spin labeling (ASL)[1] can offer superior spatial specificity[2] than BOLD fMRI. However, ASL suffers from low signal-to-noise ratio (SNR), limiting the achievable spatial resolution or demanding long scanning durations. The longer labeling duration of pseudo-continuos ASL (PCASL) offers higher SNR perfusion maps at the cost of decreased temporal resolution. In contrast, pulsed ASL (PASL) allows shorter post-labeling delays (PLD) and TRs, but has a limited bolus length and therefore SNR. Since both the temporal SNR (tSNR) and number of TRs in a run influence the fMRI statistics, we compared an optimized short-TR single-shot PASL approach to its PCASL counterpart.

Subjects/methods: Prototype PCASL/PASL background-suppressed 3D GRASE[3] sequences supporting 2D GRAPPA[4] acceleration with CAIPI[5] shifts were implemented on a MAGNETOM Prisma 3T (Siemens) with a 64-channel head coil. Experiments were performed in six healthy volunteers (3 male) after obtaining informed consent. An angiogram was used to position the labeling plane, and a subject-specific grey-matter (GM) mask was generated from a T_1-weighted MPRAGE scan. ASL parameters were: 3 mm isotropic resolution, 32 slices, single-shot 3D GRASE readout (GRAPPA 2×2, CAIPI shift = z1), optimized background suppression[5], labeling duration/PLD/TR = 1500/1580/4120 ms (PCASL) & 700/1800/2200 ms (PASL). Two 9-min functional runs were acquired during a combined unilateral flickering checkerboard and finger-tapping task that lasted for 23 s, interleaved with 40 s rest periods. The data were motion-corrected and coregistered with SPM8 before statistical analysis without spatial smoothing in FSL FEAT. Perfusion and control tSNR maps and perfusion and control tSNR efficiencies were obtained according to[7].

Results/discussion: Figure 1 shows mean PCASL and PASL 3D GRASE and control tSNR maps from one subject demonstrating the image quality and coverage. Figure 2 displays the corresponding perfusion tSNR and functional activation maps. Table 1 presents the GM results across subjects from the two methods for the perfusion and control tSNR, and the mean z-scores from the pefusion-weighted (PW) and perfusion activation (PA) maps. PCASL has higher control and perfusion tSNR than PASL leading to larger PW volume. However, the PW and PA z-scores for PASL are higher than those for PCASL, reflecting the benefit of the additional temporal samples. It should be noted that some CSF voxels had high control and perfusion tSNR in PASL, therefore correct GM identification is essential for accurate results. In conclusion, the higher tSNR of PCASL does not always guarantee outperformance and the best ASL approach for fMRI will depend on the experimental parameters.

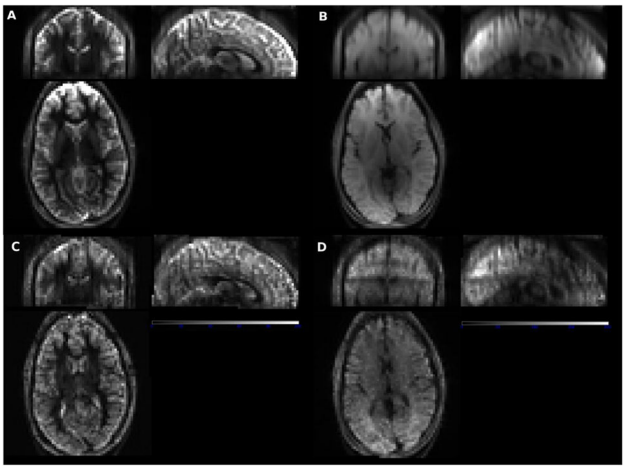

Figure1: Single-subject 3D GRASE images and control tSNR maps for PASL (A,C) and PCASL (B,D)

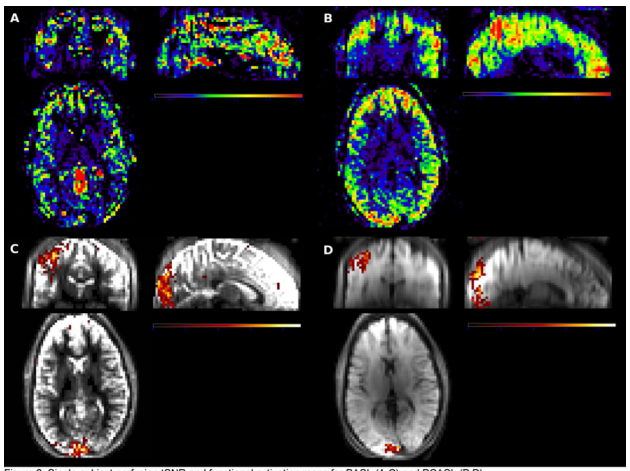

Figure 2: Single-subject perfusion tSNR and functional activation maps for PASL (A,C) and PCASL (B,D)

	Perfusion tSNR		Control tSNR		Nr. of voxels in perfusion-weighted map		Mean z-score in perfusion-weighted map		Mean z-score in visual cortex		Mean z-score in motor cortex	
	PASL	PCASL	PASL	PCASL	PASL	PCASL	PASL	PCASL	PASL	PCASL	PASL	PCASL
Subject 1	0.75	1.35	33.93	73.60	10891	14320	7.89	7.78	3.39	3.31	3.41	3.23
Subject 2	0.99	1.51	36.37	65.48	13588	15325	8.84	8.67	4.13	3.73	4.40	3.39
Subject 3	0.62	0.76	27.72	58.36	9521	11254	7.94	6.31	3.87	3.36	3.13	3.08
Subject 4	0.87	1.51	30.14	55.77	11083	15113	8.78	8.41	3.79	4.17	3.93	3.79
Subject 5	0.87	0.87	37.87	78.05	12493	15378	8.30	5.88	3.90	2.93	3.77	3.04
Subject 6	0.83	1.82	38.88	73.88	11749	15706	7.68	9.35	3.36	3.78	3.61	3.76
Average	**0.82**	**1.30**	**34.15**	**67.52**	**11554**	**14516**	**8.24**	**7.74**	**3.74**	**3.55**	**3.71**	**3.38**
Standard dev	0.13	0.41	4.44	9.10	1404	1664	0.48	1.37	0.30	0.49	0.44	0.33

Table 1: Individual and mean values in grey matter for the perfusion and control tSNR, the perfusion-weighted volume and the mean z-scores for the baseline perfusion and perfusion activation

References

1. Detre et al. MRM 1992
2. Silva et al. JCBFM 2000
3. Oshio and Feinberg. MRM 1991
4. Griswold et al. MRM 2002
5. Breuer et al. MRM 2006
6. Vidorreta et al. NMR Biomed 2014
7. Li et al. Neuroimage 2015

S06.12

Proton MRS of the foetal brain at 3T: normality

A. Viola[1], Y. Le Fur[1], P. Viout[1], S. Confort-Gouny[1], N. Girard[2]

[1]Centre de Résonance Magnétique Biologique et Médicale (CRMBM) UMR CNRS 7339, Faculté de Médecine la Timone -Aix-Marseille Université, Marseille, FRANCE, [2]Hôpital la Timone, AP_HM, Service de neuroradiologie, Marseille, FRANCE

Introduction: MRS is a non-invasive tool to assess brain metabolism in paediatric populations. Indications of foetal brain MRI represent an opportunity to study the neurochemical correlates of brain development and their alterations using ^{1}H-MRS. Since 1994 (1), only few studies have investigated normal and pathological foetal brain metabolism. We present here a ^{1}H-MRS study on the longitudinal neurochemical changes occurring in the normal foetal brain during the second and third trimesters.

Subjects/methods: Subjects: 65 foetuses with a gestational age (GA) ranging from 26 to 36 weeks were explored (Dept of Neuroradiology, La Timone Hospital, Marseille, time period: 2012–2020). The MRI/MRS protocol was carried out on a Skyra Siemens operating @ 3T with body phased-array coils and spinal coils. MRI: anatomic images with HASTE, True Fisp and T_1 GE sequences. ^{1}H-MRS: PRESS sequence, TE of 33 ms or 135 ms, TR = 1500 ms, bandwidth = 1200 Hz, 1024 points, VAPOR, NA = 96 (TE = 33 ms) or 128 (TE = 135 ms) for saturated spectra, NA = 1 for unsaturated spectra Voxel size: 6.75 cm^3 located in the deep white matter. Data post-processing with the CSIAPY software (2) under Python using a time-domain quantitation algorithm based on QUEST (3) and a simulated metabolic database created with VESPA and the GAVA (4) package allowing the analysis of metabolites and macromolecules including mobile lipids. The signals of metabolites are normalized using water signal intensity as an internal reference. Non-parametric statistics with Spearman's rank correlation were performed using JIMP software.

Results/discussion: The final data set included 44 spectra at a TE of 33 ms (mean SNR = 33, mean FWHM = 12 Hz) and 47 spectra at a TE of 135 ms (mean SNR = 30, mean FWHM = 11 Hz) (Figure 1). Spectra with artefacts (motion, eddy currents…) or outervolume contamination were discarded. Significant increases in tCr/H_2O and NAA/H_2O with GA were observed at short and long TEs ($P < 0.05$). Moreover, a significant positive correlation was found for alanine/H_2O and *scyllo*-Ins/H_2O at long echo time ($P < 0.05$).

This study corroborates previous findings on NAA and tCr obtained at 1.5T (5). These findings are in agreement with the development of dendrites and synapses, oligodendrocyte proliferation and mitochondrial activity. The use of a higher magnetic field strength permitted to gain new information on the foetal brain metabolic profile. The increase in alanine could be linked to protein synthesis whereas the role of *scyllo*-inositol in de developing brain is unknown.

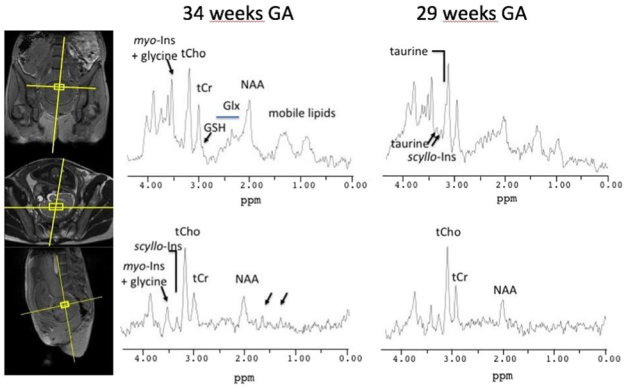

Figure 1. Typical foetal brain spectra. Abbreviations: NAA= N-acetylaspartate, tCho= total choline, tCr= total creatine, Glx= glutamine + glutamate, GSH= glutathion, myo-Ins= myo-inositol, scyllo-Ins= scyllo-inositol.

References

Mater Phys MAGMA. 2010;23(1):23–30. 3-Ratiney H, et al. NMR Biomed. 2005;18(1):1–13. 4- http://scion.duhs.duke.edu/vespa/. 5-Girard et al., Magn Reson Med. 2006 Oct;56(4):768–75. https://doi.org/10.1002/mrm.21017.

S07 Scientific Session

14:30–16:00 *Room B*

Diffusion & Perfusion

S07.01

Investigating the white matter compartmental R_2 orientational anisotropy

E. Kleban[1], C.M.W. Tax[1], M. Chamberland[1], M. Baraković[2], U. Rudrapatna[1], D.K. Jones[1]

[1]*Cardiff University, Cardiff, UNITED KINGDOM,* [2]*Ecole Polytechnique Federale de Lausanne, Lausanne, SWITZERLAND*

Introduction: The anisotropy of white matter microstructure manifests itself in various MRI contrasts. Transverse relaxation rates R_2 vary as a function of fibre-orientation with respect to the main magnetic field B_0[1–3], while the diffusion-weighted signal is modulated by the fibre-orientation with respect to an encoding gradient. Differences between intra-/extra-axonal relaxation parameters can be crucial for bio-physical interpretation of parameters extracted from diffusion experiments[4–7].

Here, we report an experimental setup which enhances the ability to investigatewhat about compartment-specific fibre-orientation dependence of R_2.

Subjects/methods: Acquisition: Five healthy subjects underwent diffusion-R_2 correlation experiments in default (0̊) and tilted (18̊) head positions on a 3T Connectom scanner equipped with a novel 20-ch head/neck tiltable coil (Fig. 1). Pre-processing: The diffusion-R_2 data were pre-processed[8–15] for each subject and head orientation. Fibre orientation distribution functions (fODFs)[16–18] were then estimated, and single-fibre-population (SFP) voxels[19] were identified and assigned to tracts or tract-segments obtained by a tractometry approach[20–23]. In SFP-voxels, we estimated the mono-exponential R_2 values from the spin-echo data at $b = 0$ s/mm^2, intra-/extra-axonal R2 values from all b-values and TEs simultaneously[4,5,7] and calculated WM fibre orientation θ to B_0. R_2 anisotropy: In SFPs across WM R_2-values were modelled as a function of θ: $R_2(\theta) = A + B\sin^2\theta + C\sin^4\theta\theta$.[24–25] Additionally, the effect of coil-orientation was visualised by comparing R_2- and $\sin^4\theta$-differences between the default and the tilted coil-orientations in each tract segment. Akaike's Information Criterion (AIC) was used to identify the best-fitting model.[26]

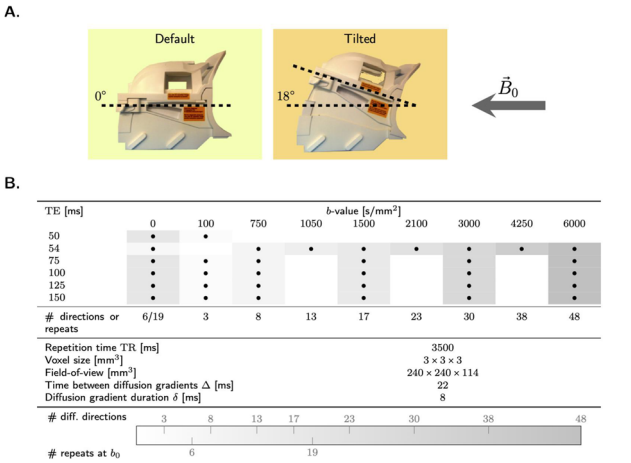

Fig1: A. Data were acquired for each participant with the coil in default (0˚) and tilted (18˚) position to B0. B. Acquisition parameters for the diffusion-R2-correlation experiment: combinations of b-values and echo times are marked with a •-symbol.

Results/discussion: In this work a tiltable receive coil was interfaced with an ultra-strong gradient scanner to allow the modulation of fibre orientation to B_0 in a robust way. The orientational anisotropy of the apparent R_2 was evident (Figs. 2, 3). A tractometry approach was applied to investigate the effect of head re-orientation on R_2-values (Fig. 3) to eliminate confounds from misregistration between coil-orientations.

This unique experimental setup introduces a new degree of freedom above traditional experiments and allows compartmental-specific R_2 orientational-anisotropy to be disentangled for the first time.

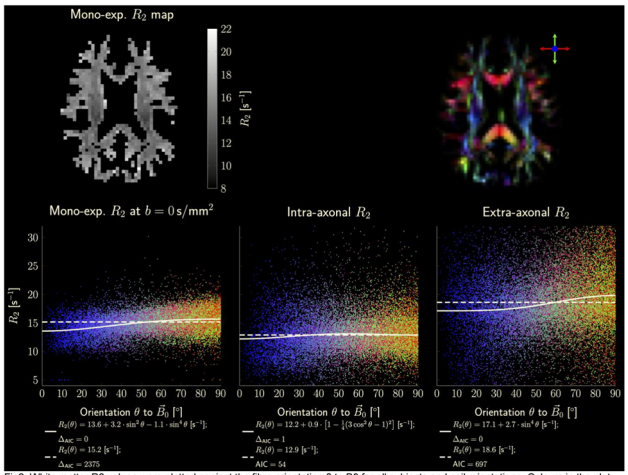

Fig2: White matter R2 values were plotted against the fibre orientation θ to B0 for all subjects and coil orientations. Colours in the plot indicate the fibre orientations from the diffusion-colormap

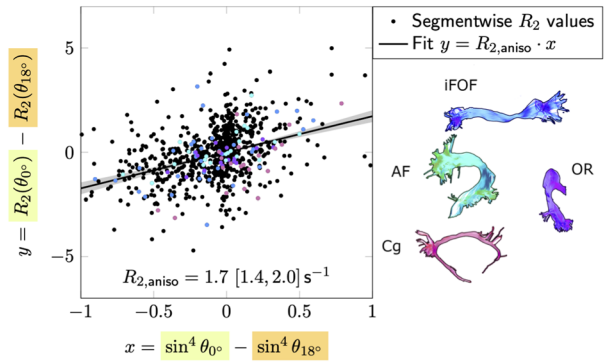

Fig3: Differences between R2 in the default (0˚) and tilted (18˚) head orientations were plotted against the corresponding differences in (sinθ)^4 for all subjects and fibre tract segments. Values for selected fibre tracts are highlighted.

References

[1]Gil et al. 2016; [2]Knight et al. 2017; [3]Knight et al. 2015; [4]Tax et al. 2017; [5]Veraart et al. 2018; [6]McKinnon et al. 2019; [7]Lampinen et al. 2020; [8]Sairanen et al. 2018; [9]Vos et al. 2016; [10]Kellner et al. 2016; [11]Andersson et al. 2003; [12]Andersson et al. 2016; [13]Glasser et al. 2013; [14]Bammer et al. 2003; [15]Rudrapatna et al. 2018; [16]Tournier et al. 2007; [17]Descoteaux et al. 2008; [18]Jeurissen et al. 2014; [19]Tax et al. 2014; [20]Bells et al. 2011; [21]Cousineau et al. 2017; [22]Chamberland et al. 2018; [23]Chamberland et al. 2019; [24]Lee et al. 2011; [25]Oh et al. 2013; [26]Akaike 1974

S07.02

A novel superficial white matter connectivity atlas of the chimpanzee brain

M. Chauvel[1], I. Uszynski[1], W. Hopkins[2], J.-F. Mangin[1], C. Poupon[1]

[1]Université Paris-Saclay, CEA, CNRS, BAOBAB, Neurospin, Gif-Sur-Yvette, FRANCE, [2]Keeling Center for Comparative Medicine and Research, The University of Texas MD Anderson Cancer Center, Bastrop, Texas, UNITED STATES

Introduction: Mapping the chimpanzee brain connectome is a key to the comprehension of the singularity of human brain evolution as it is our closest phylogenetic hominid cousin[1]. Few studies have been performed in vivo on the connectivity of chimpanzees. Bryant et al[2] published an atlas of the long structural connectivity of the chimpanzee brain. We propose here to establish an atlas of the superficial white matter (WM) connectivity in chimpanzees.

Subjects/methods: Chimpanzee cohort- A cohort of 39 chimpanzees (23 females/16 males) aged from 9 to 25 yo (National Yerkes Primate Research Center) was studied using an imaging protocol approved by the Local Animal Welfare Committee. Imaging protocol: All individuals were scanned using a Siemens 3T MRI system with a birdcage coil with a protocol including a 0.625 mm isotropic MPRAGE T1-weighted scan and a series of 5 1.9 mm isotropic diffusion MRI (dMRI) scans using a single-short 2D PGSE sequence (TE/TR = 86 ms/6 s, RBW = 1563 Hz/pix, matrix 128 × 128, FOV = 243.2 mm) at b = 1000 s/mm^2 along 60 directions. Pre/post-processing: After correcting for susceptibility artifacts and matching individuals to the Juna.Chimp template[3], dMRI data were used to compute Q-balls[4] from which a whole brain regularized deterministic tractography was launched. A fiber clustering algorithm was then applied to the obtained tractograms[5]. It includes an intra-subject hierarchical fiber clustering of connectograms, followed by an inter-subject hierarchical clustering of the individual centroid maps using the pairwise maximum Euclidean distance. Superficial clusters were finally selected using the Davi130 atlas[3] based on each couple of cortical areas, to establish a superficial WM bundle atlas of the chimpanzee.

Results/discussion: 39 individual whole brain tractograms were obtained (1503922 ± 158933 fibers across subjects), from which a fiber length histogram was computed to define length boundaries and a threshold of 40 mm to separate long from short fibers (Fig. 1). The intra-subject clustering step performed on short fibers provided 5400 ± 747 and 5473 ± 737 clusters for the left/right hemispheres respectively at the individual scale, being slightly higher for the left hemisphere.

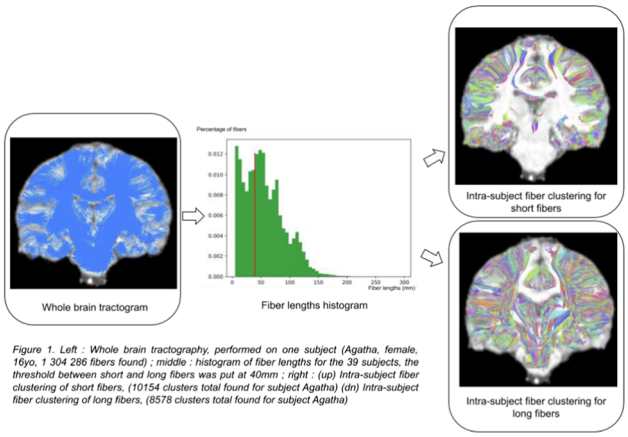

Figure 1. Left : Whole brain tractography, performed on one subject (Agatha, female, 16yo, 1 304 286 fibers found) ; middle : histogram of fiber lengths for the 39 subjects, the threshold between short and long fibers was put at 40mm ; right : (up) Intra-subject fiber clustering of short fibers, (10154 clusters total found for subject Agatha) (dn) Intra-subject fiber clustering of long fibers, (8578 clusters total found for subject Agatha)

The intersubject clustering step resulted in 302/327 clusters for the left/right hemisphere. The automatic labelling provided 259/204 clusters for the left/right hemisphere respectively, for a total of 463 clusters at the group level (Figs. 2, 3).

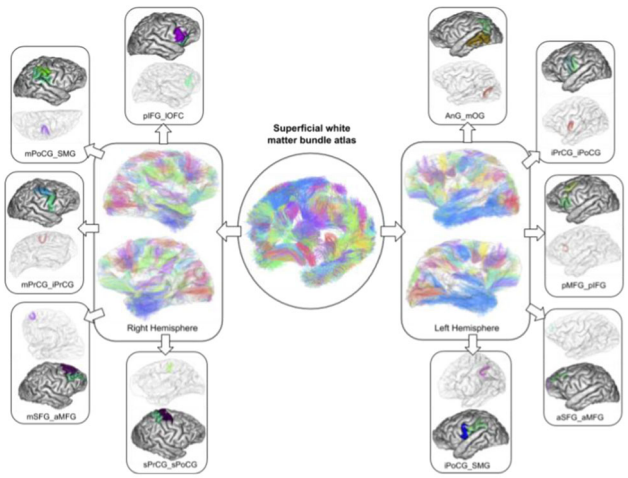

Figure 2. Superficial white matter bundle atlas (center) of the chimpanzee brain. 463 clusters were obtained, 204 on the right hemisphere (left), 259 on the left hemisphere (right), examples of found clusters are displayed around the corresponding hemispheres, with labels corresponding to the interconnected ROIs.

Left Hemisphere Atlas		Right Hemisphere Atlas	
Cortex ROI pair	#Clusters	Cortex ROI pair	#Clusters
AnG_mOG	4	AnG_sOG	4
AnG_sOG	7	SMG_AnG	7
SMG_AnG	2	SPL_AnG	3
SPL_AnG	2	SPL_SMG	2
SPL_sOG	2	SPL_sOG	2
aIFG_lOFC	4	aIFG_lOFC	4
aIFG_mIFG	1	aIFG_mOFC	2
aIFG_mOFC	1	aITG_pITG	3
aITG_pITG	9	aMFG_mIFG	2
aMFG_mIFG	3	aMFG_pIFG	2
aMFG_pIFG	3	aMFG_pMFG	3
aMFG_pMFG	2	aMTG_aITG	11
aMTG_aITG	14	aMTG_pITG	2
aMTG_pITG	5	aMTG_pMTG	1
aMTG_pMTG	4	aSFG_lOFC	1
aSFG_aMFG	7	aSFG_aIFG	2
aSTG_aITG	4	aSFG_aMFG	4
aSTG_aMTG	14	aSTG_aITG	3
aSTG_iPoCG	2	aSTG_aMTG	6
aSTG_pMTG	2	aSTG_pSTG	4
aSTG_pSTG	5	iPoCG_SMG	5
iPoCG_SMG	10	iPoCG_SPL	1
iPrCG_SMG	3	iPrCG_SMG	1
iPrCG_aSTG	1	iPrCG_iPoCG	8
iPrCG_iPoCG	7	iPrCG_mPoCG	1
iPrCG_pSTG	1	mIFG_lOFC	1
mIFG_lOFC	3	mIFG_pIFG	4
mIFG_pIFG	5	mOFC_lOFC	6
mOFC_lOFC	5	mOG_iOG	4
mOG_iOG	4	mPoCG_SMG	6
mPoCG_SMG	4	mPoCG_SPL	1
mPoCG_SPL	1	mPoCG_iPoCG	4
mPoCG_iPoCG	4	mPrCG_iPrCG	2
mPrCG_iPrCG	2	mPrCG_mPoCG	1
mPrCG_mPoCG	2	mSFG_aMFG	2
mPrCG_sPoCG	2	mSFG_pMFG	4
mSFG_aMFG	1	mSFG_pSFG	5
mSFG_pMFG	2	pIFG_lOFC	5
mSFG_pSFG	2	pIFG_iPoCG	3
pIFG_lOFC	3	pIFG_iPrCG	6
pIFG_iPrCG	2	pITG_AnG	1
pITG_AnG	1	pMFG_iPrCG	2
pITG_iOG	3	pMFG_mIFG	2
pITG_mOG	3	pMFG_mPrCG	6
pMFG_iPrCG	2	pMFG_pIFG	3
pMFG_mIFG	2	pMFG_sPrCG	3
pMFG_mPrCG	6	pMTG_AnG	3
pMFG_pIFG	3	pMTG_pITG	5
pMFG_sPrCG	3	pSFG_sPoCG	1
pMTG_AnG	5	pSFG_sPrCG	4
pMTG_aITG	3	pSTG_AnG	2
pMTG_iOG	1	pSTG_SMG	5
pMTG_mOG	8	pSTG_pMTG	2
pMTG_pITG	10	sOG_iOG	3
pMTG_sOG	3	sOG_mOG	6
pSFG_pMFG	2	sPoCG_SMG	1
pSFG_sPrCG	6	sPoCG_SPL	6
pSTG_SMG	2	sPoCG_iPoCG	1
pSTG_aMTG	2	sPoCG_mPoCG	2
pSTG_iPoCG	2	sPrCG_mPrCG	3
pSTG_pMTG	2	sPrCG_sPoCG	5
sOG_iOG	3	Total :	204
sOG_mOG	7		
sPoCG_SPL	3		
sPoCG_iPoCG	2		
sPoCG_mPoCG	4		
sPrCG_mPrCG	4		
sPrCG_sPoCG	6		
Total :	259		

Figure 3. Summary Table of the number of clusters found by ROI pairs for the two hemispheres.

We have proposed the first superficial WM atlas of the chimpanzee brain that has to be validated with post-mortem studies, which might provide a useful tool to investigate the commonalities/singularities of the chimpanzee/human brains.

References

1. Goldman et al. PNAS; 1987;84(10):3307–3311
2. Bryant et al. bioRxiv; https://doi.org/10.1101/2020.01.24.918516
3. Vickery et al. bioRxiv; https://doi.org/10.1101/2020.04.20.046680
4. Descoteaux et al. MRM; 2007; https://doi.org/10.1002/mrm.21277
5. Guevara et al. Neuroimage, 2012; 61(4), 1083–1099

S07.03

Abbreviated DWI protocol for Gaussian and non-Gaussian diffusion: application to an Alzheimer mouse model

R. Golgolab[1], D. Le Bihan[1], C. Poupon[1], M. Simonneau[2], L. Ciobanu[1]

[1]CEA, NeuroSpin, Gif-sur-Yvette, FRANCE, [2]Ecole Normale Supérieure Paris-Saclay, Département de Biologie, Gif-sur-Yvette, FRANCE

Introduction: Diffusion non-Gaussianity results from diffusion barriers and compartments created by tissue structure. Estimation of gaussian and non-gaussian diffusion is key to achieve precise tissue characterization with diffusion MRI. In this study, we introduce a simplified diffusion MRI protocol for the estimation of gaussian and non-gaussian diffusion from only 3 b-values, and we apply it to infer brain tissue alterations in an Alzheimer Disease (AD) mouse model.
Subjects/methods: Two groups of mice were used: 10 controls (WT) and 16 transgenic (AD) overexpressing human BIN1, the second most strongly Alzheimer-associated gene after APOE[1]. After sacrifice at 3 months, ex vivo diffusion images (100 µm isotropic resolution) were acquired on a 17.2T scanner using a 3D diffusion-weighted EPI sequence with three diffusion shells including 1/25/60 diffusion directions with, respectively, b0 = 0, b1 = 1500 and b2 = 4500 s/mm^2. After geometric averaging, in addition to the standard ADC (ADC1 with b0/b1 and ADC2 with b0/b2), we calculated a shifted ADC (sADC, b1/b2) which is more weighted towards non-gaussian diffusion[2]. The "gaussian diffusion limit" ADC0 (limit of ADC when b approached 0) and a non-gaussian diffusion index (NGD) (equivalent to the Kurtosis parameter, K, of the Kurtosis model) were also calculated comparing the slopes of the signal attenuation between b0-b1 (ADC1) and b1–b2 (sADC)[3] according to:

$$ADCo = sADC + (ADC1 - ADC2)(b1 + b2)/(b2 - b1)$$

$$(ADC1 - ADC2)/ADCo^2(b2 - b1) \equiv K.$$

Diffusion anisotropy was also evaluated by calculating the diffusion tensor with b1 and b2 (sFA: shifted Fractional Anisotropy). Six brain regions were investigated: hippocampus (Hippo), CA1, primary motor area (MOp), somatosensory cortex (SS), lateral septal nucleus (Spt), and corpus callosum (cc).
Results/discussion: In all regions ADC0 > ADC1 > sADC, as expected in the presence of non-gaussian diffusion. NGD values tended to be higher in the AD group compared to WT, reaching significance in MOp, SS and cc. ADC0 and ADC1 were significantly higher in the AD group in all regions, while no significant differences were found for sADC and sFA. These results suggest that early alterations in AD affect more gaussian than non-gaussian diffusion, perhaps in relation to an enlargement of extracellular spaces (fewer or smaller cells), while there is no visible impact on white matter integrity.

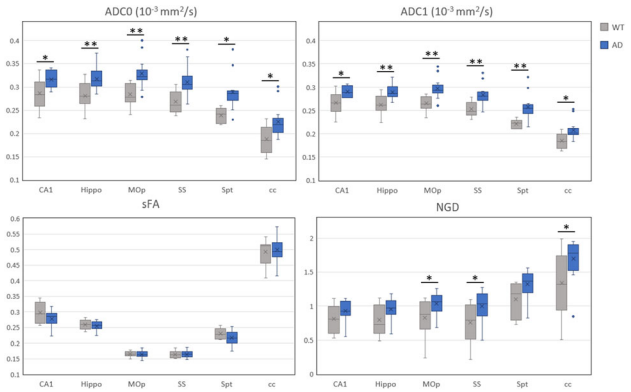

Figure 1: Boxplots of ADC0, ADC1, sFA and NGD in six brain regions, for the AD group and the WT group. *p<0.05, **p<0.005

Conclusion: Gaussian (ADC0) and non-gaussian (NGD) diffusion markers can be estimated from data acquired with only 3 b values. Without using large data sets and complex signal modelling, the ADC0/NGD approach revealed significant differences in an early stage of AD mice compared to WT mice, which could be interpreted in terms of structural alterations.

References

[1]Harold et al., Nature Genetics, 41: 1088–1093, 2009
[2]Iima M, Le Bihan, D. Radiology, 278: 13–32, 2016
[3]Le Bihan D, Ichikawa S, Motosugi U. Radiology, 285: 609–619, 2017

S07.04

Relationship between $R_2^{(*)}$ relaxation and Gd-DTPA concentration in whole blood assessed by simulations

D. van Dorth[1], L. Hirschler[1], K. Venugopal[2], B. Schmitz Abecassis[1], D.H.J. Poot[2], M. Smits[2], J.A. Hernandez-Tamames[2], M.J.P. van Osch[1]

[1]Leiden University Medical Center, C.J. Gorter Center for High Field MRI, Department of Radiology, Leiden, NETHERLANDS, [2]Erasmus University Medical Center, Radiology & Nuclear Medicine Department, Rotterdam, NETHERLANDS

Introduction: In quantitative dynamic susceptibility contrast (DSC) MRI, the concentration-time profile is generally calculated from $R_2^{(*)}$ assuming a linear relation[1]. However, the proportionality constants for tissue and arterial blood are different[2] and are dependent on the MR sequence[3]. For gradient-echo (GE) sequences a quadratic relation exists between R_2^* and Gd concentration ([Gd]) in whole blood, which is influenced by the hematocrit (HCT) value[1], while for spin-echo (SE) the relation is more complex[4] and its dependence on HCT is currently unknown.

The aim of this study is to develop and validate a simulation setup that replicates the quadratic relation between the R_2^* relaxation and [Gd] in whole blood (proof-of-concept) and to study the impact of HCT and field strength on this relation for GE and SE.

Subjects/methods: The DCE-tool of Pannetier et al. was adapted for DSC experiments (Table 1)[5]. To simulate red blood cells (RBCs), the vessel definition was used with the extravascular space corresponding to the blood plasma (geometry: Fig. 1). For the proof-of-concept the physiological parameters (Table 1) were set similar to the in vitro data as measured previously in human whole blood[1] (Fig. 1). Subsequent simulations were performed for HCT values of 10–20–30–40% and field strengths of 1.5–3–7 T (Fig. 2). To investigate the influence of the RBC shape, circles and ellipses were compared for a HCT of 29% (Fig. 3). In addition, the influence of RBC susceptibility was studied (Fig. 3).

Type	Parameter	Value
Lattice	**Dimension**	128x128 pixels (default)
	Size	70x70 μm² [5]
RBCs	**Radius**	3.5 μm [6]
	Interspace	0.6 μm [*]
	Number	Varies with HCT value (36%: 46 RBCs)
	Magnetic susceptibility	-0.0147*10⁻⁶ ppm cgs [**] [7]
	T1	1 s [***]
	T2	400*10⁻³ s [8]
Blood plasma	**Magnetic susceptibility**	0 ppm cgs
	T1	1 s [***]
	T2	90*10⁻³ s [8]
Contrast agent	**T1**	0 mM⁻¹ s⁻¹
	T2	4.6/5.2/4.8 mM⁻¹ s⁻¹ (1.5/3/7T) [9,10]
	Diffusivity	48.5*10⁻¹¹ m² s⁻¹ (default D_{free}) [5]
	Permeability	0 s⁻¹
	Magnetic susceptibility	4π*2.55*10⁻⁸ mM⁻¹ [1]
MRI	**TE**	20*10⁻³/40*10⁻³ s (GE/SE)
	TR	1 s
	Excitation time	0 s
	FA	6° [***]/90°-180° (GE/SE)
	Phase angle	0°
	Static magnetic field	1.5/3/7T
Other	**Water diffusivity**	760*10⁻¹² m² s⁻¹ (default D_{free}) [5]

Table 1: Overview of simulation parameters. *: > size of single pixel. **: oxygenated RBCs in aqueous solution. ***: to minimize T1 effects to reflect complete refreshment of flowing blood.

Results/discussion: The simulation replicated almost perfectly the previously acquired in vitro relation between [Gd] and R_2^* (Fig. 1B). As expected, the contrast increased relaxivity more for SE than GE (Fig. 1C). The quadraticity increased with HCT for both sequences (Fig. 2A, C), which was unreported so far for SE, but can be explained by water diffusion effects that are not refocused. Additionally, more RBCs result in an increased resilience against signal loss, which can explain the observed lower relaxation. For GE at low [Gd], the relaxation was higher for 10% HCT compared to 40% (Fig. 2A). This could be explained by the presence of more RBCs counteracting the effect of increased field inhomogeneities. Fig. 2B, D show an increasing relaxation with field strength, which agrees with literature[2]. The shape of the 1.5/3T curves was quadratic, while that of 7T was less uniform. The RBC shape and susceptibility had only minimal influence on R_2^* (Fig. 2E, F). In conclusion, the DCE-tool can be easily adapted to provide new detailed insight into the influence of contrast agent on the MR signal in whole blood.

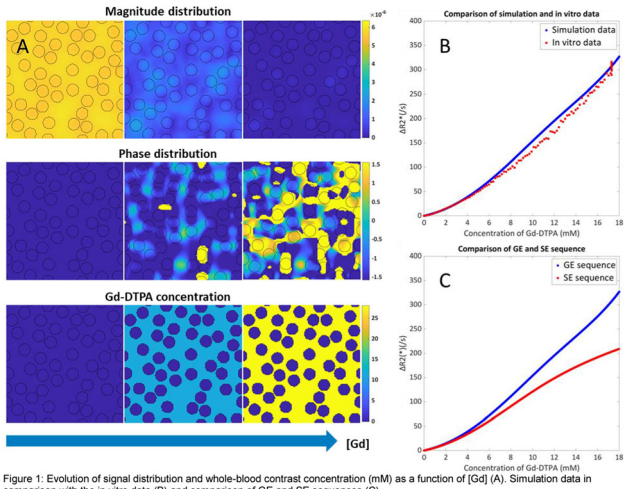

Figure 1: Evolution of signal distribution and whole-blood contrast concentration (mM) as a function of [Gd] (A). Simulation data in comparison with the in vitro data (B) and comparison of GE and SE sequences (C).

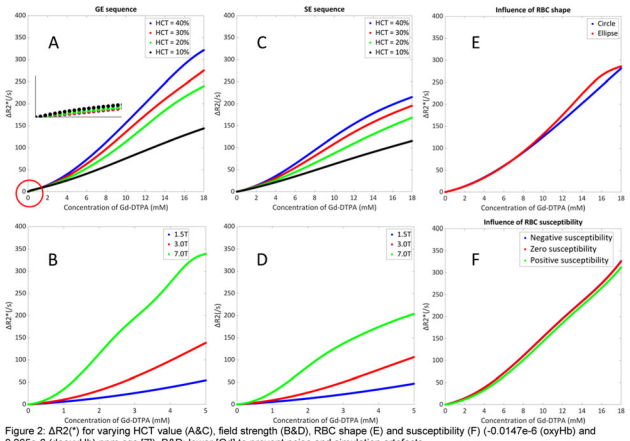

Figure 2: ΔR2(*) for varying HCT value (A&C), field strength (B&D), RBC shape (E) and susceptibility (F) (-0.0147e-8 (oxyHb) and 0.265e-6 (deoxyHb) ppm cgs [7]). B&D: lower [Gd] to prevent noise and simulation artefacts.

References

[1]van Osch, 2003, PMID: 12768585
[2]Kjølby, 2006, 16724299
[3]Kiselev, 2005, 16261568
[4]Boxerman, 1995, 8524024
[5]Pannetier, 2013, 23516414
[6]Kinnunen, 2011, 21750759
[7]Zborowski, 2003, 12668472
[8]Vidmar, 2008, 18449533
[9]Rohrer, 2005, 16230904
[10]Vignaud, 2010

We are thankful to the NWO domain AES for their support (project 17079).

S07.05

Exchange time as a proxy measure of blood brain barrier integrity: a two-stage estimation

A. Mahroo[1], J. F. Hilmer[1], N.-J. Breutigam[1], M. Chappell[2], M. Günther[1]

[1]Fraunhofer MEVIS, MR Physics, Bremen, GERMANY, [2]University of Nottingham, Precision imaging Beacon & Sir Peter Mansfield Imaging Centre, School of Medicine, Nottingham, UNITED KINGDOM

Introduction: The decreased integrity of the blood brain barrier (BBB) has been linked to many neurovascular diseases [1]. Multi-echo arterial spin labeling (ASL) offers a possibility to assess the BBB leakage by estimating the exchange time (Texch). This parameter can be estimated by harnessing the differential T2 relaxation of the spins in the blood and tissue by acquiring multiple echos (TEs) at various inflow times (TIs). However, acquiring multi-TE ASL data often results in a long scan duration.

Here, we propose a two-stage estimation of Texch by splitting the data acquisition and fitting into two stages. This approach provides improved Texch estimates and allows us to reduce the size of the multi-TE dataset which could shorten the acquisition time and make it feasible to test it in a clinical setting.

Subjects/methods: Single-TE Hadamard (HAD)-8 ASL data with seven TIs (0.6 s, 1.0 s, 1.4 s, 1.8 s, 2.2 s, 2.6 s, 3.0 s; sub-bolus: 0.45 s; repeats: 2) and multi-TE HAD-4 ASL data with three TIs (1.6 s, 2.6 s, 3.6 s; sub-bolus: 1.050 s) was simulated. Multi-TE data was generated with six TEs (0.019 s, 0.057 s, 0.095 s, 0.133 s, 0.171 s and 0.209 s). We used FSL FABBER Bayesian framework [4] to estimate all three parameters. In the first stage, single-TE data was used to estimate perfusion and arterial transit time (ATT) using the well-established Buxton model. In the second stage, these estimates were used as prior information along with the multi-TE data to estimate Texch using the two-compartment multi-TE model [3]. The two-stage estimation was compared with the single-stage HAD-8 multi-TE protocol as a reference. The reference protocol was generated with the same TIs and TEs as mentioned above. Protocols were compared using the Bayesian posterior standard deviation (SD) as a measure of estimate error and root mean square error (RMSE) relative to the ground truth values.

Results/discussion: Figure 1 shows that the proposed strategy achieved reduced perfusion and Texch estimation errors. The RMSE of the two-stage estimation provided comparable results to the reference protocol (Table 1). Fig. 2 representing the identity line plots of ATT and Texch shows that the lower Texch values were over-estimated by the proposed method.

We have demonstrated that the Texch estimation could be divided into two stages to obtain stable parameter estimates in a shorter acquisition time. Furthermore, this strategy allows us to achieve low Texch uncertainty over a wider range of ATTs. A limitation of the proposed method is over-estimation of lower Texch values. Further investigation with in vivo data is needed to establish this method.

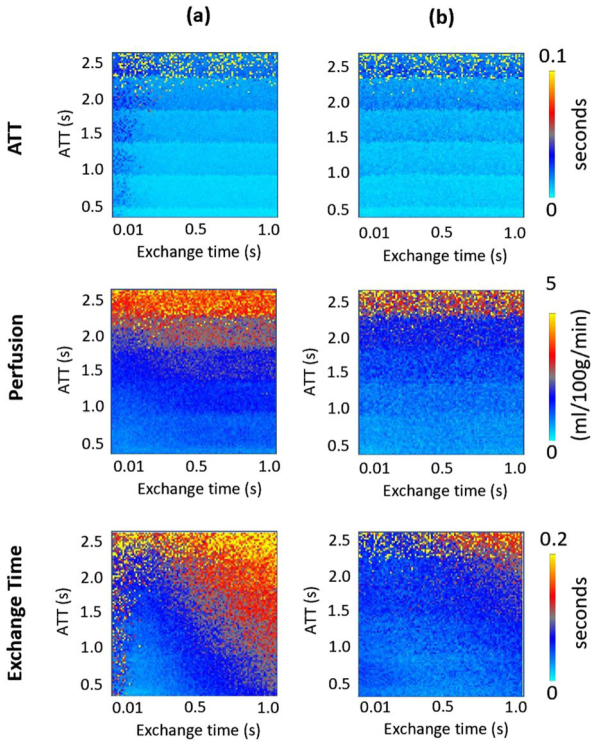

Figure 1. Standard deviation (SD) of perfusion, ATT and exchange time estimates. (a) SD of parameter estimates resulting from reference protocol. (b) SD of parameter estimates obtained from two-stage estimation.

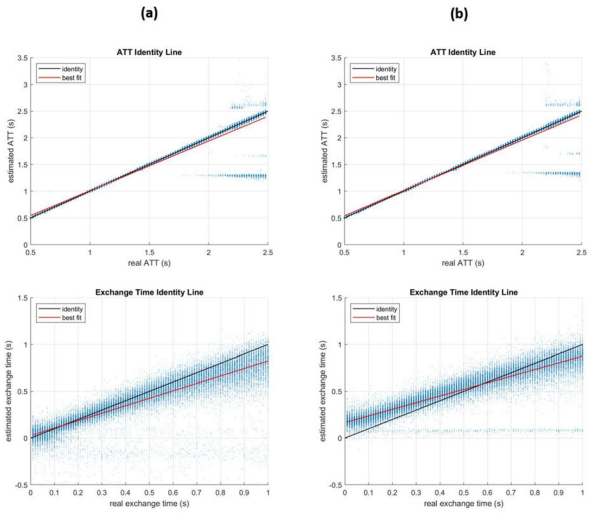

Figure 2. (a) ATT and exchange time estimated with reference protocol. (b) ATT and exchange time resulting from two-stage estimation. It shows that the lower exchange time values are over-estimated with the two-stage estimation.

Protocol	Perfusion RMSE	ATT RMSE	Exchange Time
Reference	8.229	0.179	0.175
Two-stage Estimation	8.237	0.160	0.141

Table 1. Comparison of RMSE of parameter estimates from different protocols.

References

[1] Farrall AJ, Wardlaw JM. Neurobiology of aging. 2009, 30(3):337–52

[2] Ohene Y, et al. NeuroImage. 2019, 188:515–23

[3] Gregori J, et al. Journal of magnetic resonance imaging. 2013, 37(2):332–42

[4] Chappell M.A, IEEE Transactions on Signal Processing. 2008, 57(1):223–36

S07.06

Feasibility of spatio-temporal encoding for arterial spin labelling at location with strong magnetic field inhomogeneities

M. Schuurmans[1], S. Franklin[1], M. van Osch[2], C. Bos[1]

[1]University Medical Centre Utrecht, Center for Image Sciences, Utrecht, NETHERLANDS, [2]Leiden University Medical Center, C.J. Gorter Center for High Field MRI, Department of Radiology, Leiden, NETHERLANDS

Introduction: Echo-planar imaging (EPI) is an extensively used fast acquisition method in arterial spin labeling (ASL)[1]. However, EPI faces limitations in inhomogeneous fields, because of low bandwidth in phase-encoding (PE) direction[1], which causes problems near e.g. the nasal cavities and in the abdomen. Spatio-temporal encoding (SPEN) can overcome these issues by exciting the FOV locally over time, followed by the acquisition with a blipped EPI-train. The linear relationship between spatial location and time during acquisition in the PE-direction increases the bandwidth in PE-direction and so becomes less sensitive to field-inhomogeneities. In this study SPEN was acquired in a phantom as well as in vivo combined with ASL.

Subjects/methods: A phantom (cucumber) and one volunteer were scanned on a 1.5 T Philips scanner with a single-channel coil. Phantom data was acquired using SE-EPI (FOV = 110 × 123 × 5 mm voxel size = 1.72 × 4.4 mm, TR/TE = 3000/29 ms) and SPEN (FOV = 110 × 123 × 5 mm, voxel size = 1.72 × 4.4 mm, TR/TE = 3000/52 ms). Scans were acquired with and without applying an extra field gradient of 1 mT/m. In-vivo flow alternating inversion recovery (FAIR) was combined with both SE-EPI (FOV = 244 × 244 × 5 mm, voxel size = 1.56 × 3 × 5 mm, TR/TE = 6500/91 ms) and SPEN (FOV = 200 × 200 × 5 mm, voxel size = 3 × 5.71 × 5 mm, TR/TE = 6500/52 ms). A single coronal slice was planned around the nasal cavities. Both FAIR-images used post-label delay (PLD) of 1400 ms and 10 repetitions.

SPEN reconstruction uses Fourier-transform in the read-direction and the linear relationship between acquisition-time and location in the PE-direction[2]; $y(t) = FOVy/Tacqt$ [3]. FAIR images were obtained by averaging over repetitions and subtracting label from control.

Results/discussion: Figure 1 shows the pulse sequences and Fig. 2 the SPEN and SE-EPI phantom scans, with and without additional field-gradient. SPEN proved to be robust against the induced field-inhomogeneity, while SE-EPI showed severe ghosting artifacts. Figure 3 shows the results of the FAIR scan for SPEN. The field inhomogeneity around the nasal cavities leads to deformations when using SE-EPI readout, see Fig. 3a, while no deformation is observed when using a SPEN readout, see Fig. 3b, resulting in good quality perfusion scan.

This study shows the feasibility of using SPEN as field-inhomogeneity robust method for ASL. Future studies need to improve current acquisition by enabling multi-channel coil reconstruction and improving the resolution with reconstruction algorithms of super-resolution principles[5]. Also alterations are needed to create a constant T_2-weighting over the whole image, by e.g. RASER[6]. SPEN is a promising technique to overcome the current limitations of perfusion imaging in the abdomen, like the kidneys.

References

1. Bernstein M. et al., 2004
2. Marhabaie S. et al., 2018
3. Ben-Eliezer N. et al., 2010
4. Pipe J. et al.,1995
5. Ben-Eliezer N. et al., 2010
6.Chamberlain R et al., 2007

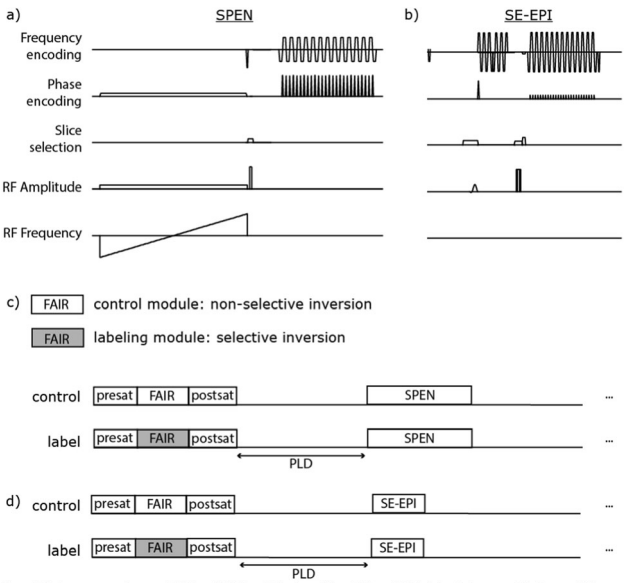

Figure 1: Pulse sequence diagram of FAIR and SPEN excitation/acquisition. A blipped EPI train/readout was used for the acquisition. Scan parameters used: Texc = 50 ms and flip angle = 90 degrees, based on numerical simulations of J. Pipe(4).

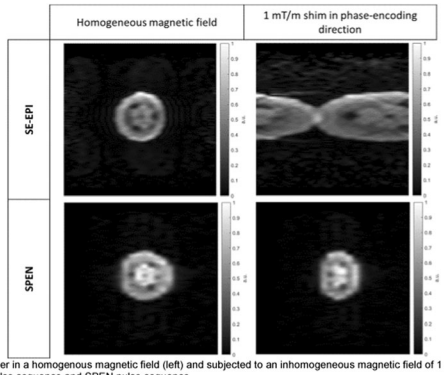

Figure 2: A cucumber in a homogenous magnetic field (left) and subjected to an inhomogeneous magnetic field of 1 mT/m (right) while applying SE-EPI pulse sequence and SPEN pulse sequence.

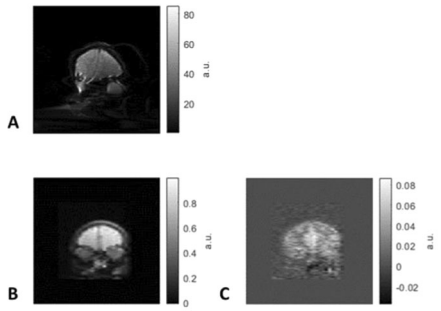

Figure 3: 3 FAIR results. A) and B) show the unsubtracted label images for SE-EPI and SPEN readout respectively. C) shows the subtracted ASL-image for SPEN readout.

S07.07

Evaluation of treatment efficacy in asymptomatic carotid artery stenosis patients by clinically applicable hemodynamic MRI and cognitive testing

S. Kaczmarz[1], J. Goettler[2], N. Sollmann[1], A. Hock[3], M. B. Hansen[4], K. Mouridsen[4], C. Zimmer[1], F. Hyder[5], C. Preibisch[1]

[1]Technical University of Munich, School of Medicine, Department of Neuroradiology, Munich, GERMANY, [2]Technical University of Munich, School of Medicine, Department of Radiology, Munich, GERMANY, [3]Philips Healthcare, Hamburg, GERMANY, [4]Aarhus University, Institute of Clinical Medicine, Aarhus, DENMARK, [5]Yale University, MRRC, New Haven, CT, UNITED STATES

Introduction: Internal carotid-artery stenosis (ICAS) is a major public health issue and accounts for 10–20% of all strokes[1]. While carotid artery stenting (CAS) and carotid endarterectomy (CEA) are available for treatment, they come with substantial stroke risks[2]. To improve treatment decisions and postoperative outcome evaluations, MR-based dynamic susceptibility contrast (DSC) imaging with relative cerebral blood volume (rCBV) and capillary transit-time heterogeneity (CTH) mapping is highly promising[3], but requires further validations[4]. Moreover, revascularization effects on known cognitive impairments[5] are widely unknown[6].

The aim of our study was therefore to evaluate the treatment efficacy in asymptomatic ICAS-patients by DSC-MRI. We hypothesized initial hemodynamic impairments and their postoperative recovery. Moreover, we investigated revascularization effects on white matter lesions (WML) and cognitive performance.

Subjects/methods: Thirty-three participants (16 asymptomatic, unilateral ICAS-patients, age = 71.4 ± 5.8y, 81% NASCET and 17 healthy controls [HC]) underwent MRI on a 3T Philips Ingenia (Best, The Netherlands) twice with 10.5 months mean follow-up time after CAS/CEA treatment. Measurements and derived parameters are summarized in Fig. 1. Median hemisphere rCBV and CTH values were calculated in GM of MCA-territories and two-sample t-tests applied. Visual attention lateralization was tested based on the theory of visual attention.[5]

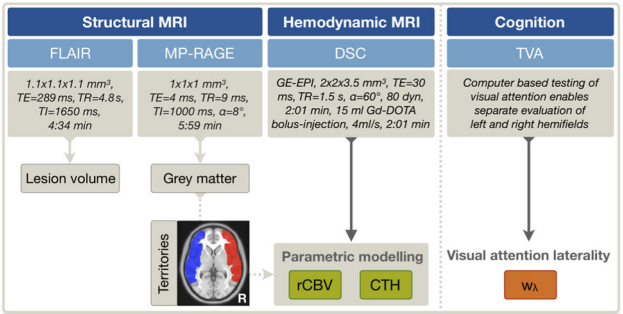

Fig.1: MRI protocol and cognitive testing. Lesion volume was segmented on FLAIR and grey matter masks on MPR. Relative cerebral blood volume (rCBV) and capillary transit-time heterogeneity (CTH) were derived by parametric DSC modelling. Lateralization of hemodynamic parameters (green) were compared in GM of MCA territories (blue & red). Besides, visual attention w_λ was tested based on theory of visual attention (TVA, orange). All measurements were performed twice, in ICAS before and after treatment.

Figure 1

Results/discussion: Exemplary ICAS-data is shown in Fig. 2. On group-level, CTH was ipsilaterally increased by +21.4% ($p < 0.01$) and rCBV by +4.3% ($p < 0.03$, Fig. 3A). Those lateralizations postoperatively recovered by ≈ 80%, reaching hemispheric symmetry ($p > 0.4$). WML increased non-significantly by +12.7% (Fig. 3B). Initially impaired visual attention (22% lateralization, $p < 0.01$) did not improve after treatment ($p > 0.7$, Fig. 3C). All HC parameters were symmetrical in both scans.

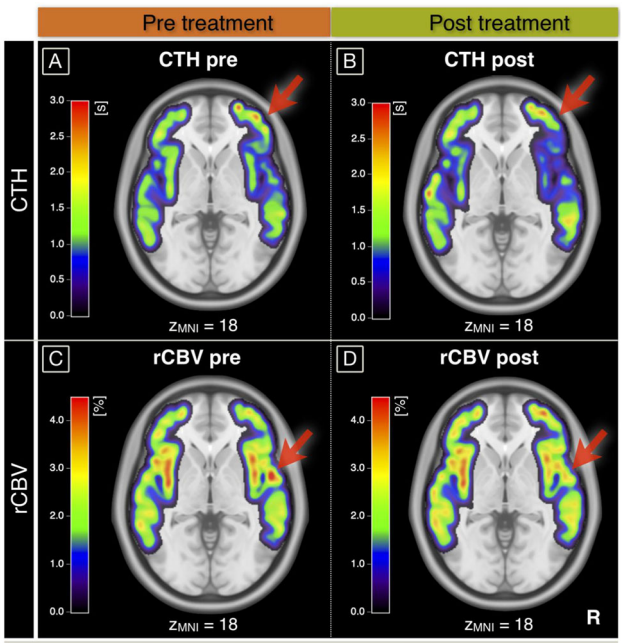

Fig.2: Exemplary data of a right-sided ICAS-patient. Maps of CTH (A,B) and rCBV (C,D) maps are compared before (A,C) and after treatment (B,D). All MNI-normalized maps are overlaid on a $T1_W$-Atlas and corresponding axial positions are noted. The GM & MCA territory masked maps were smoothed for illustration. After treatment, ipsilateral CTH and rCBV elevations decreased (arrows). For group level analyses, median parameter values of unsmoothed maps per hemisphere were evaluated.

Figure 2

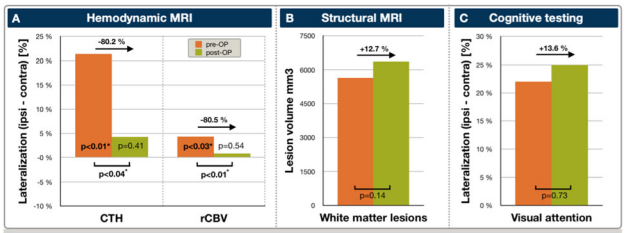

Fig.3: Hemodynamic, structural and cognitive changes after ICAS-treatment. Parameters were evaluated in ICAS-patients before (orange) and after treatment (green). Lateralizations of CTH and rCBV recovered after treatment (A). While matter lesions slightly increased postoperatively (B). Cognitive testing based on TVA revealed persisting visual attention lateralization wλ deficits (C). Relative parameter changes after treatment are noted on top of each graph. Asterisks indicate significant differences, assessed by two-sample t-tests with p<0.05.

Figure 3

As hypothesized, hemodynamics were initially impaired in ICAS and recovered postoperatively, while the HC results affirmed specificity. In ICAS, ipsilateral rCBV increases indicate chronic vasodilation[7], which normalized after treatment. CTH impairments imply capillary dysfunction.[3] Its postoperative recovery agrees with reported short-term effects[8]. Contrary, visual attention remained impaired, in line with previous results[6]. This might be due to counteracting positive effects of CTH recovery[9] vs. negative effects of micro emboli during treatment[10], in coherence with WML increases.

To summarize, DSC is highly promising to clinically assess the individual hemodynamic status within 2 min. While hemodynamic impairments recovered, cognitive impairments postoperatively persisted in ICAS.

References

1. Petty, Stroke, 1999
2. Rond, Stroke, 2003
3. Jespersen, JCBFM, 2012
4. Marshall, Stroke, 2018
5. Göttler, JCBFM, 2019
6. Schröder, NICli, 2019
7. Derdeyn, Brain, 2002
8. Arsava, EStroke, 2018
9. Ostergaard, CurNRep, 2015
10. Maggio, CerVas, 2017

S07.08

Comparing the repeatability of cerebrovascular reactivity measurements using PET/MRI

M. Zhao[1, 2], A. Fan[3], D. Chen[4], M.M. Khalighi[2], G. Zaharchuk[2]

[1]Stanford University, The Richard M. Lucas Center for Imaging, Stanford, UNITED STATES, [2]Stanford University, Department of Radiology, Stanford, UNITED STATES, [3]University of California Davis, Department of Biomedical Engineering and Neurology, Davis, UNITED STATES, [4]Shuang-Ho Hospital, Taipei Medical University, Department of Radiology, Taipei, TAIWAN

Introduction: Cerebrovascular reactivity (CVR) reflects the change in cerebral blood flow (CBF) in response to a vasoactive stimulus. Studies have demonstrated that CVR has the potential to become an important biomarker to assess cerebrovascular diseases [1]. CVR can be derived using both PET and MRI based techniques in which a stress-test is performed using such stimuli as acetazolamide (ACZ) [2]. However, these techniques are not widely applied in clinical studies because the repeatability has not been fully examined.

Here, we investigate the repeatability of CVR using [^{15}O]-Water PET/MRI. Inter-session and inter-subject variations of the CVR measurements were assessed using within-subject coefficient of variation (wCV) and between-subject coefficient of variation (bCV).

Subjects/methods: PET/MRI data were collected on a 3T PET/MRI scanner (GE SIGNA, Waukesha, WI, USA) from twelve healthy volunteers (43 ± 18 years, seven female). All imaging experiments were conducted in two sessions separated by 7–15 days. The mean amount of [^{15}O]-water injected was 880 MBq. ACZ was administered at a dose of 15 mg/kg of body weight (maximum 1 g). Single post-label delay (PLD) PCASL (PLD = 2025 ms, bolus duration = 1450 ms, NEX = 3), multi-PLD PCASL (PLD = 700, 1325, 1950, 2575, 3200 ms, bolus duration = 2000 ms, NEX = 1), and PET data were acquired using the sequence parameters described in [3]. Phase contrast (PC) MRI and T1-weighted structural images were collected. ASL MRI CBF was quantified by fitting the data to the general kinetic model. PET CBF was estimated using the PC-PET method using the flow volume estimated from the PC data [4]. CVR was computed as the percentage of CBF change with respect to baseline CBF. wCV and bCV were calculated in six ROIs using the techniques in [5]. A lower wCV and higher bCV are preferred due to the implication of lower variability in repeated measurements and higher specificity in different subjects.

Results/discussion: Figure 1 shows the estimated CVR map of an example subject. Overall, good repeatability was achieved for all three techniques. Figure 2 shows the CVR of each ROI. No significant CVR differences were identified between the two sessions, although the mean CVR from PET was significantly higher than the ASL-based CVR in all ROIs. Figure 3 shows the wCV and bCV. The wCV of PET were lower than for MRI in all ROIs while the bCV of PET was the highest. PET-based CVR technique demonstrated higher repeatability due to its lower wCV.

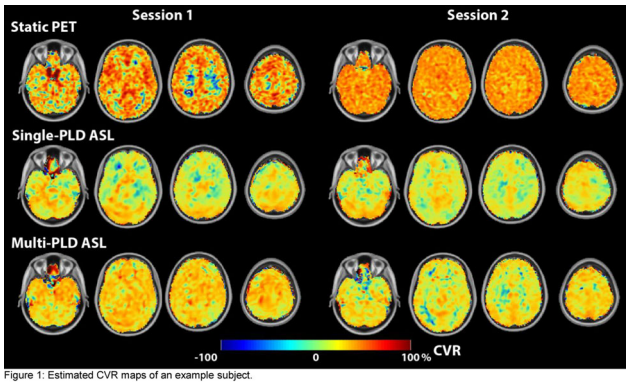

Figure 1: Estimated CVR maps of an example subject.

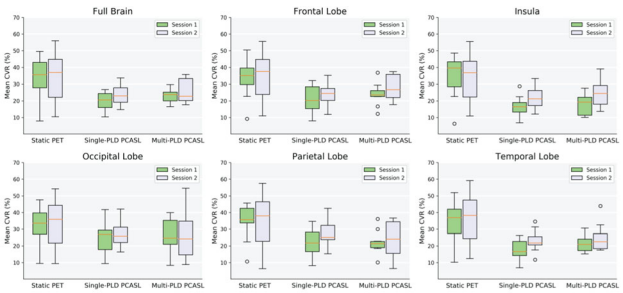

Figure 2: Mean CVR of PET and ASL MRI techniques in six ROIs.

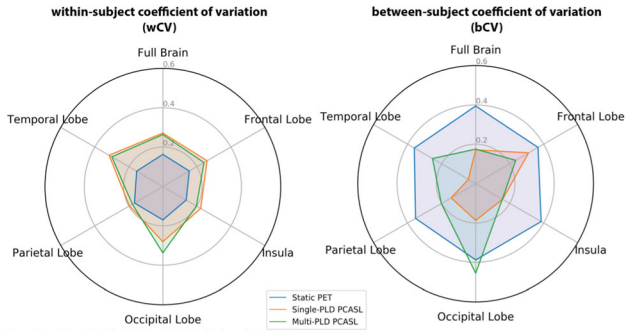

Figure 3: wCV and bCV of PET and MRI techniques in six ROIs.

References

1. P. Liu, et al., Neuroimage 2019
2. M Zhao, et al., MRM 2020
3. A Fan, et al., Stroke 2017
4. Y Ishii, et al., JMRI 2019
5. A Cohen, et al., JMRI, 2019

S07.09

Comparison of diffusion-weighted imaging (DWI), perfusion-weighted imaging (PWI) and MR spectroscopy (MRS) as a biomarkers for therapy response after stereotactic radiosurgery in patients with recurrent glioblastoma multiforme (GBM): our experience

P.P. Arcuri[1], S. Roccia[2], A. Quattrone[3], M. F. Spadea[4], E. Mazzei[5], G. Fodero[1]

[1]A.O. Pugliese Ciaccio, Radiology "De Lellis", Catanzaro, ITALY, [2]A.O. Pugliese Ciaccio, Medical Direction, Catanzaro, ITALY, [3]University "Magna Graecia" of Catanzaro, Department of Neurology, Catanzaro, ITALY, [4]University "Magna Graecia" of Catanzaro, Department of Clinical and Experimental Medicine, Catanzaro, ITALY, [5]A.O. Pugliese Ciaccio, Radiotherapy, Catanzaro, ITALY

Introduction: Glioblastoma (GBM) is the most common primary malignant brain neoplasm with an incidence of 4/100,000. GBM accounts for 54% of all glial tumors and 45% of all malignant central nervous system (CNS) tumors. Prognosis of patients with GBM is dismal with a median survival of 14–16 months, and a survival rate of < 30 and 10% at 2–5 years after the initial diagnosis, respectively. Accurate differentiation of true progression (TP) from pseudoprogression (PsP) in patients with GBMs is essential for planning adequate treatment and for estimating clinical outcome measures and future prognosis. The purpose of this study was to investigate the correlation of post-treatment quantitative advanced magnetic resonance imaging (DWI, PWI and MRS) methods in distinguishing TP from PsP in GBM patients.

Subjects/methods: 36 patients with recurrent GBM after chemoradiation therapy (CRT) were evaluated retrospectively. Baseline MRI and early two follow-up examinations were acquired every 3–5 months using dynamic contrast enhancement (DCE), perfusion MRI and ^{1}H-MR spectroscopic imaging. Kruskal–Wallis non-parametric test was performed. Cho/Cr and Cho/NAA ratios were normalized to corresponding metabolite ratios from contralateral normal parenchyma and compared between TP and PsP groups. Maps of relative cerebral blood volume (rCBV) and apparent diffusion coefficient (ADC) were coregistered with choline (Cho) and N-acetyl-aspartate (NAA) concentrations and compared to usually used relative parameters as well as responders patients. Sensitivity, specificity and accuracy were assessed. Fisher's exact test was used to evaluate statistical significance. A p value < 0.05 was considered statistically significant. Histology or radiological and clinical follow-up was the gold standard reference.

Results/discussion: Multiparametric imaging helped to differentiate features of tumour progression from radiation-related changes. A low apparent diffusion coefficient (ADC) $< 1 \times 10^{-3}$ mm^2/s, high relative cerebral blood volume (rCBV) ratio > 2.3, high choline/creatine (Cho/Cr) ratio > 1.9 suggested tumor recurrence. A high ADC $> 1 \times 10^{-3}$ mm^2/s, low rCBV ratio < 2.3, Cho/Cr ratio < 1.9 suggested SRS-induced radiation changes. Sensitivity, specificity and diagnostic accuracy were respectively: rCBV = 82%, 79%, 81%; ADC = 75%, 73%, 79%; Cho/Cr ratio = 76%, 80%, 82. Post-treatment rCBV may be used as imaging biomarker to help predict long-term response of recurrent glioblastoma multiforme (GBM).

References

1. Mohan S, Chawla S, Wang S, Verma G, Skolnik A, Brem S, Peters KB, Poptani H. CNS Oncol. 2016 Jul;5(3):137–44.
2. Reardon DA, Ballman KV, Buckner JC, Chang SM, Ellingson BM. Neuro Oncol. 2014 Oct;16 Suppl 7:vii24–35.
3. Stadlbauer A, Pichler P, Karl M, Brandner S, Lerch C, Renner B, Heinz G. Eur J Radiol. 2015 Jun;84(6):1128–36
4. Stupp R, Taillibert S, Kanner A, Read W, Steinberg D, Lhermitte B, et al. JAMA. (2017) 318:2306–16